Influence of negatively charged plume grains on the structure of Enceladus' Alfvén wings: Hybrid simulations versus Cassini Magnetometer data

Hendrik Kriegel,[1] Sven Simon,[2] Uwe Motschmann,[1,3] Joachim Saur,[2] Fritz M. Neubauer,[2] Ann M. Persoon,[4] Michele K. Dougherty,[5] and Donald A. Gurnett[4]

Received 17 May 2011; revised 18 July 2011; accepted 23 July 2011; published 20 October 2011.

[1] We apply the hybrid simulation code AIKEF (adaptive ion kinetic electron fluid) to the interaction between Enceladus' plume and Saturn's magnetospheric plasma. For the first time, the influence of the electron-absorbing dust grains in the plume on the plasma structures and magnetic field perturbation, the Alfvén wing, is taken into account within the framework of a global simulation. Our work continues the analytical calculations by Simon et al. (2011), who showed that electron absorption within the plume leads to a negative sign of the Hall conductivity. The resulting twist of the magnetic field, referred to as the Anti-Hall effect, has been observed during all targeted Enceladus flybys between 2005 and 2010. We show that (1) applying a plume model that considers both, the neutral gas and the dust allow us to quantitatively explain Cassini Magnetometer (MAG) data, (2) dust enhances the anti-Saturnward deflection of the ions, causing asymmetries which are evident in the MAG data, and (3) the ions in the plume are slowed down below 1 km s^{-1}; and we compare our results to MAG data in order to systematically analyze variations in the plume activity and orientation for selected pairs of similar flybys: (E5, E6), (E7, E9) and (E8, E11).

Citation: Kriegel, H., S. Simon, U. Motschmann, J. Saur, F. M. Neubauer, A. M. Persoon, M. K. Dougherty, and D. A. Gurnett (2011), Influence of negatively charged plume grains on the structure of Enceladus' Alfvén wings: Hybrid simulations versus Cassini Magnetometer data, *J. Geophys. Res.*, *116*, A10223, doi:10.1029/2011JA016842.

1. Introduction

[2] Six years ago, Saturn's small icy moon Enceladus (R_E = 252.1 km) was found to be highly active due to the extensive plume of water vapor and dust below its south pole [*Dougherty et al.*, 2006; *Spencer et al.*, 2006; *Tokar et al.*, 2006; *Spahn et al.*, 2006; *Waite et al.*, 2006; *Hansen et al.*, 2006]. The plume consists of several collimated jets, which originate from hot spots within the "tiger stripes" [*Spitale and Porco*, 2007]. The gaseous part of the plume was measured by Cassini's Ion and Neutral Mass Spectrometer (INMS) to consist of about 90% H_2O [*Waite et al.*, 2006, 2009], which leaves the surface vents at supersonic speeds (Mach number of M = 1.5 or even higher) [*Hansen et al.*, 2008, 2010]. Simulations and modeling of INMS and UVIS data yield a plume source strength of 10^{27}–10^{28} H_2O s^{-1}, that is 30–300 kg s^{-1} [*Tian et al.*, 2007; *Smith et al.*, 2010; *Tenishev et al.*, 2010].

[3] The neutral gas of the plume is partially ionized and Saturn's magnetospheric plasma is slowed down by the interaction with the plume due to charge exchange (momentum loading) and mass loading via photoionization and electron impact ionization. The deceleration and deflection of the impinging magnetospheric plasma near the plume of Enceladus leaves a measurable imprint on the magnetic field topology [see, e.g., *Dougherty et al.*, 2006]. Specifically, the interaction generates a system of Alfvén wings, which have already been studied extensively through theoretical modeling and observations [see, e.g., *Neubauer*, 1980, 1998; *Saur et al.*, 1999; *Khurana et al.*, 2007, and references therein]. The theory of the sub-Alfvénic interaction has been extended with respect to the asymmetry caused by Enceladus' south polar plume by *Saur et al.* [2007]. They propose an additional hemisphere-coupling current system to be present at Enceladus due to the partial blockage of the field-aligned currents by the solid body of the moon. These currents cause discontinuities in the magnetic field which were recently identified in the Cassini Magnetometer (MAG) data by *Simon et al.* [2011].

[4] Enceladus' plasma interaction has already been studied through several global numerical simulations: by using a

[1]Institute for Theoretical Physics, TU Braunschweig, Braunschweig, Germany.
[2]Institute of Geophysics and Meteorology, University of Cologne, Cologne, Germany.
[3]Institute for Planetary Research, German Aerospace Center (DLR), Berlin, Germany.
[4]Department of Physics and Astronomy, University of Iowa, Iowa City, Iowa, USA.
[5]Space and Atmospheric Physics Group, Blackett Laboratory, Imperial College London, UK.

0148-0227/11/2011JA016842

multifluid model, *Saur et al.* [2008] found evidence for a temporal variability of the plume source strength between Cassini flybys E0, E1 and E2. They determined the neutral production rate to be as high as $7 \times 10^{27} - 5 \times 10^{28}$ H_2O s^{-1}. Their study as well as our previous hybrid simulation study [*Kriegel et al.*, 2009] show reasonable agreement with MAG data and indicate a different tilt of the plume for the E1 and E2 flybys. By comparison of hybrid simulations with Cassini Plasma Spectrometer (CAPS) data from the E3 encounter, *Omidi et al.* [2010] found that the plume density at the south pole is of the order of 5×10^8 cm^{-3}, corresponding to a production rate of ~4 kgs^{-1} of new ions. *Jia et al.* [2010b, 2010c] systematically analyzed the influence of the different ionization mechanisms on Enceladus' plasma interaction by applying an MHD model. They determined the production rate for E0–E6 to be in the range of $(2.2–3.2) \times 10^{28}$ H_2O s^{-1}.

[5] Recently, a significant imbalance between the number densities of free electrons and ions ($n_e < 0.1 n_i$) has been observed within the plume [*Farrell et al.*, 2009] and during E-ring crossings [*Wahlund et al.*, 2009]. This void in the electron density has shown to be associated with electron absorption by submicron dust grains [*Yaroshenko et al.*, 2009]. This dust population can be considered another plasma species since its Debye length is large compared to the average distance between the grains [*Shafiq et al.*, 2011].

[6] *Simon et al.* [2011] extended the analytical theory of the Alfvén wing with respect to the presence of negatively charged dust. They showed that electron absorption by submicron dust grains within the plume has a drastic influence on the magnetic field configuration in Enceladus' Alfvén wings. If the density of the free and mobile electrons drops below a certain threshold, the Hall conductivity assumes a negative sign. *Saur et al.* [1999, 2002] demonstrated that the Hall effect in sub-Alfvénic plasma interaction rotates the electric and magnetic field and other plasma properties. The presence of electron-absorbing dust reverses this direction of rotation as shown by *Simon et al.* [2011], who referred to it as "Anti-Hall effect". The impact of the Anti-Hall effect manifests in the orientation of the magnetic field perturbation perpendicular to the background field and the corotation direction. By approximating the plume by a cylinder with constant height-integrated conductivities, they succeeded in qualitatively reproducing magnetic field data obtained by Cassini during flybys E3–E9.

[7] In contrast to what is claimed in recent literature [*Jia et al.*, 2010a, 2010b, 2010c], it is therefore *not* necessary to account for the large-scale, centrifugally driven dynamics of the flux tubes in Saturn's magnetosphere in order to understand magnetic field observations within the Enceladus plume. However, for a realistic description of Enceladus' magnetospheric interaction, (at least) three plasma species need to be taken into account: electrons, water group ions, and the dust grains, where the dust grains include a wide distribution of charge-to-mass ratios.

[8] In the present paper, we therefore continue the work of *Simon et al.* [2011] and present the first simulation study of the influence of charged dust on the structure of Enceladus' Alfvén wings. In particular, we extend our previous hybrid model of Enceladus' plasma interaction [*Kriegel et al.*, 2009] such that we now include momentum loading via charge exchange as well as the electron absorption by dust. The following problems are addressed:

[9] 1. We analyze the asymmetric ion flow deflection caused by the presence of negatively charged dust, since *Simon et al.* [2011] studied only the influence of electron absorption on the magnetic field.

[10] 2. We compare Cassini magnetometer data with our simulation results for a realistic neutral plume model *and* including negative dust.

[11] 3. Based on this comparison, we estimate variations in plume activity and possible tilt for flybys E5–E9 and E11.

[12] The paper is organized as follows: in section 2, we give an overview of the theoretically expected magnetic field structures, Cassini flybys at Enceladus and MAG data obtained during them. In section 3, we present our model and explain how electron absorption by dust can be included in the hybrid approach. In section 4, the model is validated by comparing a simplified test scenario against the analytical calculations of *Saur et al.* [1999] and *Simon et al.* [2011]. Moreover, the asymmetric flow deflection due to Hall- and Anti-Hall effect is discussed. In section 5, the 3D structures of Enceladus' plasma interaction are discussed along with an analysis of Cassini MAG data for selected pairs of similar flybys: (E5, E6), (E7, E9) and (E8, E11). Finally, we provide a summary in section 6.

2. Enceladus' Alfvén Wings and MAG Data

[13] The coordinate system used for the flybys and the simulations is the Enceladus Interaction System (ENIS). Its ($+x$) axis is aligned with the direction $\underline{u}_0$ of ideal corotation, whereas the ($+z$) axis points northward, thereby being approximately antiparallel to the ambient magnetospheric field $\underline{B}_0$. The ($+y$) axis completes the right-handed coordinate system and points toward Saturn, antiparallel to the convective electric field $\underline{E}_0 = -\underline{u}_0 \times \underline{B}_0$ of the upstream plasma. The origin of the ENIS system coincides with the center of Enceladus.

2.1. Enceladus' Alfvén Wings

[14] The sub-Alfvénic interaction of a conducting obstacle, such as Enceladus' plume, can be illustrated as follows: ion-neutral collisions and mass loading within the plume give rise to Pedersen and Hall currents within the local interaction region. These currents are closed by a system of currents which form the Alfvén wing. These currents flow at an angle θ_A to the background field $\underline{B}_0$ toward Saturn's northern and southern ionosphere, where θ_A is measured from $\underline{B}_0$ in corotation ($+x$) direction. The corresponding bending of the field lines yields a negative B_x component in the northern and a positive one in the southern wing. In addition, the Hall current within the plume gives rise to a component along the Saturn-Enceladus-line (B_y). In the far field (i.e., where the magnetic field arising from Pedersen and Hall currents can be neglected), the wing current system and the associated magnetic field perturbations exhibit translation symmetry along the wing characteristics. This also implies that the orientation of the B_y component, even at large distances to Enceladus, is determined by the value of the Hall conductivity in the local interaction region. An illustration of the wing will be presented together with the results in Figure 2.

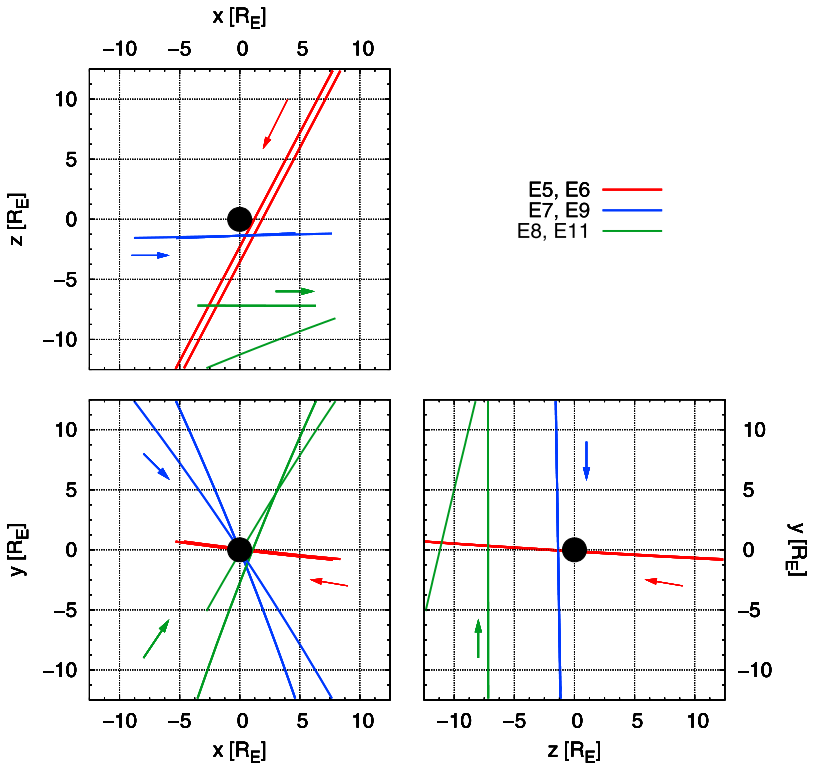

Figure 1. Trajectories of Enceladus flybys addressed in this paper.

[15] Based on the work of *Neubauer* [1980], *Simon et al.* [2011] give the magnetic field perturbations as a function of the electric potential (see Simon et al.'s equations (6)–(8)). For constant height-integrated conductivities inside a cylindrical plume, the magnetic field inside the Alfvénic flux tube can be computed as a function of the height-integrated Pedersen and Hall conductivities Σ_P and Σ_H (equations (9)–(10)). Away from the obstacle (far-field solution) the B_y perturbation is then given by

$$B_y = \pm \frac{4\mu_0 E_0}{\sqrt{1+M_A^2}} \frac{\Sigma_A^2 \Sigma_H}{\Sigma_H^2 + (\Sigma_P + 4\Sigma_A)^2}, \quad (1)$$

where Σ_A denotes the Alfvén conductance, M_A the Alfvénic Mach number and E_0 the convective electric field in the upstream plasma. Here, the upper sign and lower sign correspond to the northern and southern wing, respectively. Obviously, the sign of the B_y component is determined by the sign of the Hall conductance:

$$\begin{array}{lll} \Sigma_H > 0 & \rightarrow & B_y \gtrless 0, \\ \Sigma_H < 0 & \rightarrow & B_y \lessgtr 0. \end{array} \quad (2)$$

Simon et al. [2011] showed that the Hall conductance Σ_H becomes negative, if the dust grains of number density n_D are charged with ξ electrons and fulfill

$$\xi n_D > n_i \frac{\nu_{in}^2}{\nu_{in}^2 + \Omega_i^2}, \quad (3)$$

with n_i, ν_{in} and Ω_i being the ion density, the ion-neutral collision frequency and the ion gyrofrequency, respectively. With the ENIS system being the frame of reference, the Hall current is then carried almost exclusively by the ions, reversing its direction and thereby the corresponding sign of the Hall conductivity. Thus, strong electron absorption by dust grains reverses the orientation of the B_y component within the Alfvén wings.

[16] In that work, the perpendicular currents were assumed to be distributed uniformly in z direction. In reality, however, the neutral density and thus, the collision frequency decrease with distance to Enceladus' south pole. Therefore, the model of *Simon et al.* [2011] does not include a realistic description of the magnetic pile-up in front of the plume, as visible in the B_z component. Moreover, their model can only handle a plume geometry that exhibits cylindrical symmetry around the z axis. Therefore, comparing the magnetic field signatures obtained from that model to observations does not allow constraint of the shape, density or especially a possible tilt of the plume, as indicated by *Kriegel et al.* [2009]. These gaps are filled by the present study.

2.2. Cassini Flybys and MAG Data

[17] Since a detailed description of most of the flybys and the MAG data has been provided by *Khurana et al.* [2007], *Jia et al.* [2010a] and *Simon et al.* [2011], we will only give a brief summary here.

[18] Until the end of 2010, Cassini had accomplished 14 targeted flybys of Enceladus. The first of these encounters (E0, E1 and E2 in 2005) occurred upstream of the moon, i.e., the spacecraft did not pass through the center of the Alfvénic flux tube. The second sequence of encounters (E3–E6 in 2008) were downstream flybys, with Cassini

traveling through the near-Enceladus region steep from north to south. During a third sequence of encounters (E7–E9), Cassini passed again through the plume from downstream to upstream while moving parallel to the moon's orbital plane at $z = -1.5\ R_E$ (E7 and E9) and $z = -7.5\ R_E$ (E8), respectively. E10 had a similar trajectory as E1. The E11 encounter was similar to E8, but had a small northward tilt of about 15° against the equatorial plane and was even further south ($z \approx -11\ R_E$). The two most recent encounters, E12 and E13 at the end of 2010, were both north polar flybys parallel to the equatorial plane. For the reader's convenience, the trajectories of all flybys used in this paper (E5–E9, E11) are shown in Figure 1.

[19] For all flybys except for E8 and E11, Cassini observed a negative B_x perturbation, indicating that the spacecraft passed through the center of the northern Alfvén wing although it was located below the south pole for many of the flybys. This means that Cassini crossed the interaction region *between* the south pole of Enceladus and the region where the momentum loading rate achieved its peak value. During all these flybys, the B_y perturbation exhibited a negative sign. During E8 and E11, the spacecraft flew through the southern Alfvén wing and the measured magnetic field perturbation was positive for both, B_x and B_y. As stated above, the measured orientation of B_y is therefore indicative of strong electron absorption by dust. Surprisingly, for the component in the direction of the background field (B_z), only a negative perturbation was measured during all flybys so far. Since the background field has always $B_z < 0$, Cassini passed only through regions of enhanced $|\underline{B}|$. In other words, the spacecraft intersected the magnetic pile-up region, but did not penetrate the corresponding magnetic cavity in the downstream region.

3. Hybrid Model

[20] In this work, we study the plasma interaction of Enceladus by applying a three-dimensional, quasi-neutral hybrid model. The hybrid approach treats the electrons as a massless, charge-neutralizing fluid. Since the ions are represented by individual particles, the model can handle multiple ion species and does not need to make any assumptions on the velocity distribution of the ions. Our simulation code AIKEF (Adaptive Ion Kinetic Electron Fluid) [*Müller et al.*, 2011] is the successor of the "Braunschweig Code" which has been applied to the plasma interaction of various objects in the solar system, e. g. comets [*Bagdonat and Motschmann*, 2002; *Motschmann and Kührt*, 2006], Mars [*Bößwetter et al.*, 2004] and the Saturnian satellites Titan [*Simon et al.*, 2006, 2007], Rhea [*Roussos et al.*, 2008] and Tethys [*Simon et al.*, 2009]. Recently, AIKEF has also been used for real-time simulations of Titan'smagnetopause crossing during the T32 flyby [*Müller et al.*, 2010] as well as the lunar ARTEMIS flyby [*Wiehle et al.*, 2011].

[21] The simulation code used in our previous study of Enceladus' plasma interaction [*Kriegel et al.*, 2009] has now been extended to a parallelized version, using a hierarchical grid. In contrast to that study, we now include negatively charged dust and momentum loading via charge exchange in addition to mass loading. Since the basics of the code have been described in detail in the aforementioned studies, we will only give a brief overview and focus on the modifications and parameters which are necessary to describe the plasma interaction of Enceladus.

3.1. Field Equations and Basic Assumptions

[22] We will quickly review the general derivation of the equation for the electric field to show how a negatively charged dust/ion species is treated within the framework of the hybrid model.

[23] We consider a plasma consisting of electrons and $\alpha = 1, .., n$ ion and dust species. Charge neutrality then reads

$$\sum_{\alpha} q_\alpha n_\alpha = e n_e, \tag{4}$$

with q_α being the charge and n_α being the number density of species α. Using the definition of the current $\underline{j}$ and rearranging for the electron velocity $\underline{u}_e$ yields

$$\underline{u}_e = \frac{\sum_\alpha q_\alpha n_\alpha \underline{u}_\alpha - \underline{xj}}{e n_e} = \frac{\sum_\alpha q_\alpha n_\alpha \underline{u}_\alpha - \underline{j}}{\sum_\alpha q_\alpha n_\alpha}, \tag{5}$$

where $\underline{u}_\alpha$ denotes the bulk velocity of species α. This expression can be inserted into the electron momentum equation for zero electron mass in order to get the generalized equation for the electric field in the hybrid model:

$$\begin{aligned}\underline{E} &= -\underline{u}_e \times \underline{B} - \frac{\nabla P_e}{e n_e} + \eta \underline{j} \\ &= -\frac{\sum_\alpha q_\alpha n_\alpha \underline{u}_\alpha}{\sum_\alpha q_\alpha n_\alpha} \times \underline{B} + \frac{(\nabla \times \underline{B}) \times \underline{B}}{\mu_0 \sum_\alpha q_\alpha n_\alpha} - \frac{\nabla P_e}{\sum_\alpha q_\alpha n_\alpha} + \eta \frac{\nabla \times \underline{B}}{\mu_0},\end{aligned} \tag{6}$$

where $\underline{B}$ denotes the magnetic field and P_e the electron pressure. In the derivation of the latter equation, we also used Ampère's law and neglected the displacement current. The last term describes the diffusion of the electromagnetic fields through a medium of finite resistivity, such as the moon's solid body, where $\eta = 1/\sigma$ (σ, electric conductivity) [see *Kriegel et al.*, 2009]. The time evolution of the magnetic field can be obtained by applying Faraday's law to equation (6). The set of equations is completed by an adiabatic law for the electron pressure.

[24] In this study, we consider one single-charged water group ion species and dust charged with ξ electrons: $q_1 = e$, $q_2 = -e\xi$. The electric field then finally writes as

$$\begin{aligned}\underline{E} = &-\frac{n_i \underline{u}_i - \xi n_D \underline{u}_D}{n_i - \xi n_D} \times \underline{B} + \frac{(\nabla \times \underline{B}) \times B}{\mu_0 e (n_i - \xi n_D)} - \frac{\nabla P_e}{e (n_i - \xi n_D)} \\ &+ \eta \frac{\nabla \times \underline{B}}{\mu_0}.\end{aligned} \tag{7}$$

Thus, the hybrid model is capable of describing a negatively charged ion/dust species. We only have to ensure that the electron density is always larger than zero (i.e., $\xi n_D < n_i$). For numerical stability, we set a minimum electron density of $n_e = n_i - \xi n_D \geq 10\%\ n_0$, where n_0 is the upstream ion

density. We would like to note that if one includes only one single-charged ion species (i.e., $\xi n_D = 0$), the first term simplifies to $\underline{E} = -\underline{u}_i \times \underline{B}$.

3.2. Ion Motion and Charge Exchange

[25] The motion of the ions is governed by the Lorentz force. In addition, an ion of species α could react with a neutral molecule A of the plume, producing an ion of species β and a neutral of species B according to

$$\alpha^+ + \mathrm{A} \longrightarrow \beta^+ + \mathrm{B}. \tag{8}$$

β^+ and B can have arbitrary velocities consistent with momentum and energy conservation after the encounter. The occurrence of the ion-neutral reactions is described statistically by a Poisson distribution. Therefore, the probability that an ion survives a time t without a reaction is given by

$$P(t) = \exp\left(-\frac{t}{\tau}\right), \tag{9}$$

where τ is the average time between reactions, depending on the cross section $\sigma(v_{rel})$ for the respective reaction, the neutral density $n_n(\underline{x})$ at the particle's position $\underline{x}$ and its velocity v_{rel} relative to the neutral. Instead of the cross section, often the reaction rate coefficient $k_{\alpha\beta} = \sigma(v_{rel})\, v_{rel}$ is used for a given velocity range. The probability that an ion undergoes a reaction in the next time interval dt is then given by $p\, dt$ with

$$p = \frac{d}{dt}(1 - P(t))\bigg|_{t=0} = \frac{1}{\tau} = \sigma(v_{rel}) n_n(\underline{x}) v_{rel} = k_{\alpha\beta}\, n_n(\underline{x}), \tag{10}$$

where $P(t = 0) = 1$, since the particle "lives" at the beginning of the time interval. The corresponding quantity used in the description of the Alfvén wing in section 2.1 is the ion-neutral collision frequency $\nu_{in} = \tau^{-1}$.

[26] These statistical reactions are implemented in AIKEF by calculating the reaction probability $p\, \Delta t$ for each particle within the next numerical time step Δt and comparing it against a random number $r \in [0; 1]$. If $p\, \Delta t > r$, the ion undergoes a reaction and is deleted, while a new one of species β is created. The initial velocity of the new particle is set to the velocity $\underline{u}_n$ of the neutrals.

[27] At Enceladus, the upstream plasma consists mainly of O^+, OH^+, H_2O^+ and H_3O^+ [*Tokar et al.*, 2006, 2008]. In the present study, however, we consider only a single species of water group ions ($\alpha^+ = \beta^+ = W^+$), which reacts with the neutral water molecules of the plume ($A = H_2O$). Assuming that all upstream ion species have roughly equal abundances [*Tokar et al.*, 2006], the major reactions listed in the auxiliary material of *Fleshman et al.* [2010] yield an average rate of $k_{\alpha\beta} = k_{W^+} = 2.2 \times 10^{-9}$ cm^3 s^{-1}.

[28] We would like to note that the net effect of the reactions between the water group ions and water is a deceleration of the plasma in the rest frame of Enceladus, since $|\underline{u}_n| < |\underline{u}_i|$, but no change in the total mass of the plasma occurs, as all reaction partners have a similar mass. Therefore, the reactions and charge exchange processes at Enceladus can be referred to as *momentum loading* in contrast to photoionization and electron impact ionization (*mass loading*), which are included in our model as well.

[29] According to the neutral density and the ionization rate, new ions are inserted into the simulation. The photoionization rate for water is $\nu_{photo} = 4.4 \times 10^{-9}$ s^{-1} at 9.5 AU for quiet solar conditions [*Burger et al.*, 2007]. This rate is kept spatially constant, since none of the flybys discussed here occurred in Saturn's geometric shadow and the plume is assumed to be optically thin. The electron impact ionization is mainly carried by a warm ($k_B T_e \sim 100$ eV) electron population with a rate coefficient of $I_e = 4.5 \times 10^{-8}$ cm^3 s^{-1} [*Fleshman et al.*, 2010]. In agreement with Fleshman et al., we set the fraction of the warm electrons in the upstream flow to 0.5% of the total electron density. This population also contributes to the electron pressure (equation (7)). We neglect any variations in the local ionization rate due to the energy loss of the electrons when moving through the plume.

3.3. Modeling the Plume

[30] We model the neutral density according to the single-plume model given by *Saur et al.* [2008]. The density profile is given by

$$n_n(r, \vartheta, \varphi) = n_{n,0} \left(\frac{R_E}{r}\right)^2 \exp\left[-\left(\frac{\vartheta}{H_\vartheta}\right)^2\right] \exp\left[\frac{R_E - r}{H_d}\right], \tag{11}$$

where $n_{n,0}$ denotes the base density on Enceladus' surface. The parameters r and ϑ are the radial distance from the center of Enceladus and the polar angle, respectively. H_ϑ denotes the angular width of the plume. The third term arises from the gravitation of Enceladus. We set H_d equal to the Hill radius of 948 km.

[31] Simulations based on Cassini UVIS measurements suggest that the neutrals ejected from the south polar regions have a surface density on the order of 10^{10}–10^{11} cm^{-3} [*Tian et al.*, 2007]. This base density is related to the plume production rate Q according to

$$n_{n,0} = \frac{Q}{A u_n R_E^2}, \tag{12}$$

where $A = 0.054$ is an integration constant due to the opening angle of the plume [see *Jia et al.*, 2010c]. Assuming a neutral speed of $u_n = 1$ km s^{-1}, a surface density of 10^{10} cm^{-3} corresponds to a plume production rate of 3×10^{28} H_2O s^{-1}.

[32] Measurements and simulations indicate a variation in the activities of the jets [*Saur et al.*, 2008; *Kriegel et al.*, 2009; *Teolis et al.*, 2010; *Tenishev et al.*, 2010; *Smith et al.*, 2010]. Therefore, $n_{n,0}$ is treated as a free parameter to model the source strength for the individual flybys. We vary $n_{n,0}$ between different simulation runs in steps of 1×10^{10} cm^{-3}.

[33] *Spitale and Porco* [2007] showed that the plume consists of at least eight jets. However, *Saur et al.* [2008] showed that a multiplume model might not be necessary to reproduce MAG data. The effect of the single jets on the global shape of the plume is mainly given by variations in the location of active regions, which may yield a global tilt of the plume. For each flyby, we therefore tested different tilts of the plume in order to achieve best possible agreement with MAG data. In the ENIS system, the symmetry axis of the plume has the direction ($\cos\varphi_0 \sin\vartheta_0$, $\sin\varphi_0 \sin\vartheta_0$, $\cos\vartheta_0$), with $\varphi_0 \in [0°; 360°]$ and $\vartheta_0 \in [90°; 180°]$. These

angles correspond to planetographic latitude (Lat) and longitude (Lon) on Enceladus' surface as follows: $90° - \vartheta_0$ = Lat(°) and the correlation between φ_0 and Lon is given by (0° ≙ 90°W, 90° ≙ 0°W, 180° ≙ 270°W, 270° ≙ 180°W). Please note that the angle φ_0 is measured in counterclockwise direction (with respect to the ENIS system), whereas the value of Lon increases when moving clockwise around Enceladus. Since these additional parameters strongly increase the number of necessary simulations, we at first checked, if a tilt of the symmetry axis toward planetary latitudes of −80° along the $\pm x$ and $\pm y$ axis yielded any notable improvement when comparing our results with Cassini MAG data. If that was the case, we further varied the latitude in steps of $\vartheta_0 = 5°$ and the longitude in steps of $\varphi_0 = 22.5°$ to find the optimal set of parameters.

[34] From UVIS observations during a star occultation on 24 October 2007, *Hansen et al.* [2008] obtained a Mach number of the gas of about $M = 1.5$, which is in agreement with simulations [*Tian et al.*, 2007; *Smith et al.*, 2010; *Tenishev et al.*, 2010]. Assuming a gas temperature of 150 K (that is a thermal speed of $v_{th} = 455$ m s^{-1}), this yields an outgassing velocity of $u_n = 680$ m s^{-1}. More recent data suggest a even higher velocity of $M = 4$ [*Hansen et al.*, 2010]. A Mach number in the range of 1.5–4 corresponds to opening angles of the individual jets of $\arctan(v_{th}/u_n) = 30° - 15°$. However, as we use a single-plume model, the opening angle H_ϑ includes both, ejection speed and location of the vents. We found that our simulations yield a considerably better agreement with a more confined plume and therefore set $H_\vartheta = 7.5°$ (see also section 5.2). With regard to the dynamics of the ions, however, we found that a neutral velocity on the order of 1 km s^{-1} does not have a noteworthy influence on the outcome of the simulation. For simplicity, we therefore neglect the neutrals' velocity in the ionization processes, i.e., the newly generated ions start with initial velocity zero.

3.4. Dusty Plasma Parameters

[35] According to *Farrell et al.* [2010] and *Shafiq et al.* [2011], the charged submicron-sized dust grains in the Enceladus plume may be considered an additional plasma constituent, since the inter-grain distance for dust densities of $n_D \geq 10^{-1}$ cm^{-3} is smaller than the effective dusty plasma Debye length of $\lambda_{Eff} \sim 1$ m. Assuming spherical grains with a mass density of $\rho = 10^3$ kg m^{-3} (water ice) and an average number of $\xi = 50$ electrons for a grain size of 0.03 μm and $\xi = 8000$ for a grain size of 1 μm, the charge-to-mass ratio ranges from $q_D/m_D = 3 \times 10^{-1}$ C kg^{-1} to $q_D/m_D = 7 \times 10^{1}$ C kg^{-1} [*Shafiq et al.*, 2011]. Therefore, we consider the charged dust as an additional plasma species with a charge-to-mass ratio of $q_D/m_D = 5.5$ C kg^{-1} $= 10^{-6}\, q_{W^+}\, m_{W^+}$. These parameters are consistent with the estimations of *Simon et al.* [2011]. Due to this small charge-to-mass ratio, this averaged dust species does practically not move during the simulation runtime, which is on the order of a few minutes. We would like to note that this would still be true for nanometer-sized grains with a significantly larger charge-to-mass ratio of $q_{D,nm}/m_{D,nm} \sim 10^{-4}\, q_{W^+}/m_{W^+}$, since the accelerating electric field is strongly reduced within the center of the plume (see section 5). Moreover, the resulting dust charge density can also be interpreted to include a fraction of positively charged grains as reported by *Jones et al.* [2009], because only the total dust charge density is taken into account by our simulations. The presence of positively charged grains would then just mean that the density of the negative grains is even larger.

[36] The source strength of the dusty part of the plume is characterized analogously to the gas plume by the density $\xi n_{D,0}$ of charged dust at the south pole, which is varied in steps of 50 cm^{-3}. We would like to note that we only describe a stationary density profile of the *charged* dust in our model, while a self-consistent model of the electron absorption is out of the scope of this paper and will be addressed in future work. The implications of this approximation are discussed in section 4.3 of *Simon et al.* [2011]. The spatial density profile of the dust is similar to the neutral density profile (equation (11)). However, due to the ejection speeds of the dust grains being comparable to the escape velocity of Enceladus, the influence of gravitation and inertia forces is larger for the dust grains than for the gas, leading to complicated trajectories around Enceladus [*Kempf et al.*, 2010]. We account for that by setting $H_\vartheta = 15°$ for the dust. Moreover, the charging time depends on grain size and the ambient plasma conditions. Therefore, the spatial profile of the dust *charge* density in the plume may be different from the profile of the dust *number* density. We find that our results are in better agreement with Cassini MAG data, if we replace the geometric r^{-2} decrease (see equation (11)) by r^{-1}. The resulting profile does not claim to be a quantitatively realistic image of the charged dust population at Enceladus. That would require a much more sophisticated model of the grain-size-distribution of the dust, the dust motion in the three-body-problem and the dust charging process, which is by far out of the scope of this paper.

3.5. Simulation Parameters and Geometry

[37] The physical background conditions are similar to the parameters used in our previous study [*Kriegel et al.*, 2009]: the upstream plasma is assumed to consist of water group ions with an average mass of $m_i = 17.5$ amu, flowing at the ideal corotation velocity of $\underline{u}_0 = (26.4,0,0)$ km s^{-1} relative to Enceladus. We would like to note that recent data [*Wahlund et al.*, 2005, 2009; *Wilson et al.*, 2009] show evidence for a sub-corotation of the upstream flow, whereas our assumption of ideal corotation was mainly made to improve numerical stability. However, this does not affect our conclusions, since we are interested in the general plasma structures and *relative* variations of the plume.

[38] The ion temperature has been set to $k_B T_i = 35$ eV [*Sittler et al.*, 2006]. *Wahlund et al.* [2009] also reported on the detection of a cold ion population that is nearly stationary compared to Enceladus. This population has not yet been included in the model. The electron pressure includes contributions from two electron populations: a warm population with $k_B T_{ew} = 100$ eV, which makes up a fraction of 0.5% of the total electron density and a cold population. Measured values for the temperature $k_B T_{ec}$ of the cold electron population range from 1.35 eV [*Sittler et al.*, 2006] to 2.3 eV [*Gustafsson and Wahlund*, 2010]. In agreement with our previous work we choose $k_B T_{ec} = 1.35$ eV. The background magnetic field is approximated by a dipole field which is fitted to the unperturbed upstream field of the respective flyby. At the center of Enceladus, the field is approximately given by $\underline{B}_0 = (0, 0, -325$ nT). Since the

Table 1. Physical and Numerical Parameters Used in the Simulations

Parameter	Symbol	Value
Plasma velocity	u_0	26.4 km s^{-1}
Plasma number density	n_0	45–90 cm^{-3}
Magnetic field at (0, 0, 0)	B_0	(0, 0, −325) nT
Ion mass	m_i	17.5 amu
Alfvénic Mach number	M_A	0.1–0.15
Ion temperature	$k_B T_i$	35 eV
Cold electron temperature	$k_B T_{ec}$	1.35 eV
Hot electron temperature	$k_B T_{eh}$	100 eV
Density fraction of hot electrons		0.5% n_0
Opening angle (gas plume)	H_ϑ	7.5°
Opening angle (dust plume)	H_ϑ	15°
Charge exchange rate coefficient	k_{W^+}	2.2×10^{-9} cm^3 s^{-1}
Photoionization rate	ν_{Ph}	4.4×10^{-9} s^{-1}
Electron impact rate coefficient	I_e	4.5×10^{-8} cm^3 s^{-1}
Mesh spacing L_0	Δ_{L_0}	53 km = 0.21 R_E
Mesh spacing L_2	$\Delta_{L_2} = \frac{1}{4}\Delta_{L_0}$	13 km = 0.05 R_E
Box size (x and y)	L_x, L_y	20 R_E
Box size (z)	L_z	70 R_E

number density of the plasma varies with SKR longitude [*Gurnett et al.*, 2007] from 45 to 90 cm^{-3}, it is set individually for each flyby. For E5/E6 and E8, the upstream densities measured by Cassini's Radio and Plasma Wave Science Instrument (RPWS) are given by *Jia et al.* [2010b] and *Gurnett et al.* [2011], respectively. The upstream densities of the other flybys were also obtained by taking averages of RPWS electron densities. The applied values are listed in Table 2.

[39] The size of our simulation box is 20 × 20 × 70 R_E. Because of the south-polar plume and the associated structures, Enceladus is not placed at the center of the box, but at 4/7 of the box height. We use a hierarchical mesh that is adaptive in space but static in time, with up to three levels of refinement: L_0, L_1, L_2. At the coarsest level (L_0), the resolution is Δ_{L_0} = 53 km = 0.21 R_E, while it is $\Delta_{L_2} = \frac{1}{4}\Delta_{L_0}$ = 13 km = 0.05 R_E in the highest level. The spatial extension of the refinement levels is illustrated by the plots of our mesh in Figures 4a and 4d. Due to limited computational resources, we were not able to perform every simulation with the highest resolution, but only the final (best fit) runs. All other runs are carried out using a mesh with only two levels of refinement (L_0, L_1), since we did not notice a remarkable dependency of our results on the grid resolution. The ions and the dust are represented by macroparticles, possessing the same mass-to-charge-ratio as the real particles [*Bagdonat*, 2004]. In each cell we have 100 macroparticles per species, yielding a total of more than one billion macroparticles in the simulation. To improve the numerical stability without any smoothing procedure, we also set a value of $\eta = 1.4 \times 10^3$ m S^{-1} in the plasma outside the obstacle. At all outer boundaries of the simulation box, new particles are continuously inserted into the simulation according to a drifting Maxwellian velocity distribution (inflow boundaries for particles), while the fields are extrapolated from neighbor cells (outflow boundaries for fields). In order to prevent the Alfvén wings from being reflected back at the ±z boundaries (as reported by *Omidi et al.* [2010]), we damp the wings distant from the interaction region. This is done by setting a higher η near the boundaries above $z = +20$ R_E and below $z = -30$ R_E. The interior of Enceladus is modeled self-consistently without any inner boundary condition for the electromagnetic fields by a resistivity of $\eta = 2 \times 10^6$ m S^{-1}, as described by *Kriegel et al.* [2009]. This high value of the resistivity enforces the radial component of the current at the surface of Enceladus to almost vanish, as demanded by equation (27) of *Neubauer* [1998]. The physical and numerical parameters are summarized in Table 1. For further numerical details, the reader is referred to *Müller et al.* [2010, 2011].

4. The Influence of Negatively Charged Dust on the Structure of the Alfvén Wings

[40] In this section, we demonstrate that our hybrid model is able to reproduce the correlation between the signs of B_x and B_y, as observed in the Alfvén wings of Enceladus. In order to show the principle effect of the electron-absorbing dust, we keep the interaction scenario as simple as possible: a plasma of water group ions undergoes collisions with a constant collision frequency $\nu_{in} = 0.5\ \Omega_i$ within a cylindrical volume, where Ω_i is the ion gyrofrequency. The upstream conditions are identical to the "real" Enceladus scenario (see Table 1). The cylinder with height 4 R_E and radius 3 R_E is centered at the origin of the ENIS system, while the solid body of Enceladus is *not* included in this test scenario. Furthermore, the cylinder is filled with a uniform density $\xi\ n_D$ of negative dust, which is treated as an additional plasma species. From equation (3), we expect the Anti-Hall effect to occur for dust charge densities of $\xi n_D > 0.2 n_i$. Therefore, we consider two different cases: $\xi n_D = 0$ (case 1) and $\xi n_D = 2n_i/3$ (case 2).

[41] Figure 2 shows the results without any dust (case 1) in Figures 2a, 2c, and 2e compared to those with $\xi n_D = 2/3 n_i$ (case 2, Figures 2b, 2d, and 2f). Figures 2a and 2b show the B_y component of the Alfvén wings generated by the cylindrical obstacle. One can clearly see the small inclination angle of the Alfvén wing against the background field of arctan $M_A = 7°$. The effect of the dust is best illustrated by the currents parallel to the Alfvén characteristics ($\approx j_z$) in a plane perpendicular to the wings, shown here at $z = +7.5$ R_E (compare Figures 2e and 2f). With zero Hall effect, i.e., for $\xi n_D = 0.2 n_i$, the maximum of these currents would be located at the y axis [*Saur et al.*, 1999]. For $\xi n_D = 0$, the Hall effect rotates these currents clockwise, while a dust charge density of $\xi n_D = 2n_i/3$ causes a rotation counterclockwise (Anti-Hall effect) [*Simon et al.*, 2011]. The resulting B_y component is displayed for both cases in the same plane (see Figures 2c and 2d). It can clearly be seen from Figures 2a–2d that in the interior of the northern Alfvén flux tube, B_y is positive without and negative with dust. Within the southern wing, the opposite situation occurs. Outside the flux tube, the wing-aligned currents yield a quadrupole-like structure of the B_y component.

[42] For this simple scenario, we can quantitatively compare the hybrid model results with the theory discussed by *Simon et al.* [2011]: Their equations (29) and (32) allow calculation of the conductivities, and using their equations (6)–(10), the corresponding constant magnetic field perturbations in the far field inside the flux tube. In case 1, we get a Pedersen conductance of Σ_P = 14 S, a Hall conductance of Σ_H = 7 S and B_y = ±5 nT (positive: north,

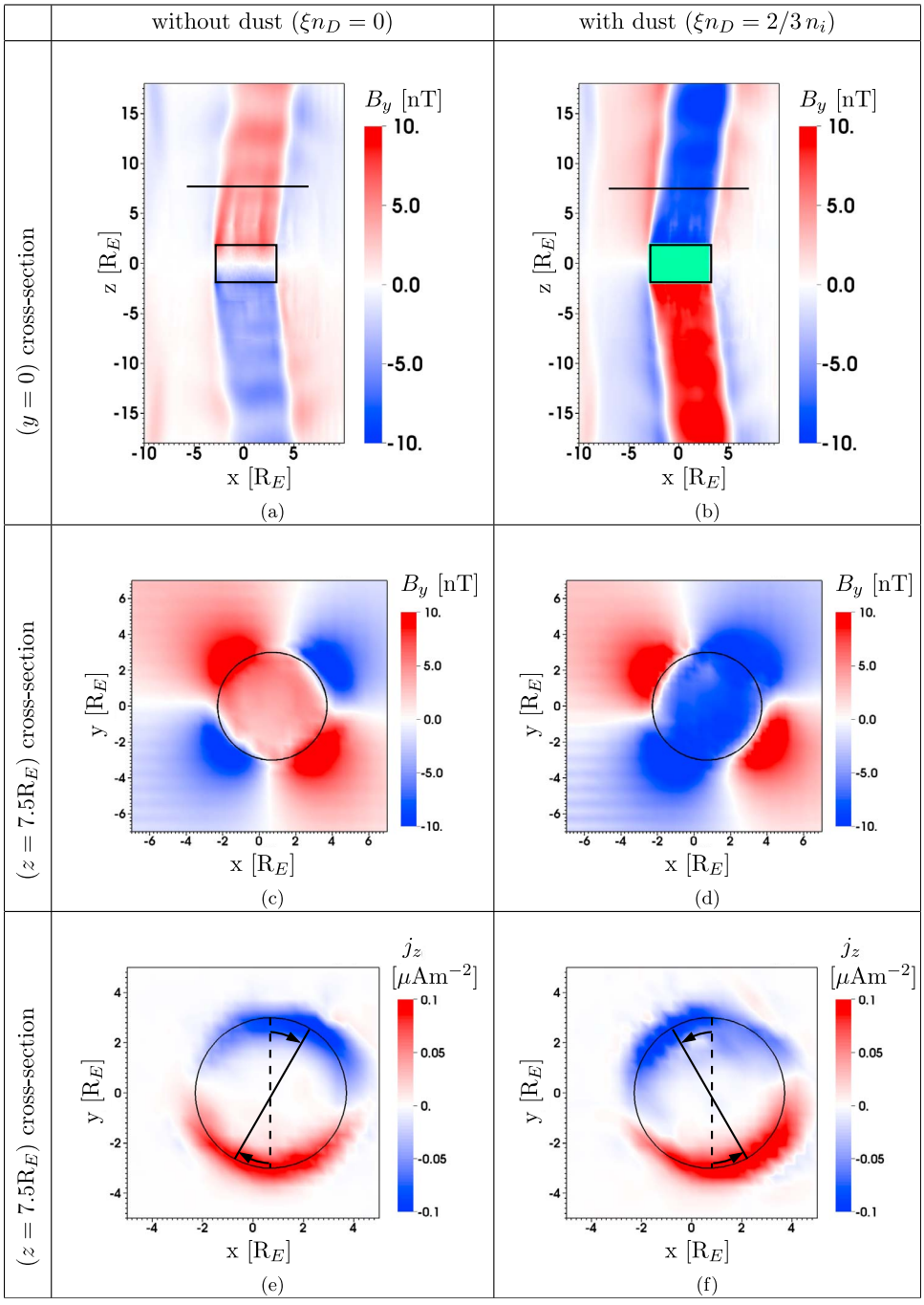

Figure 2. Results from hybrid simulations in order to show the principle effect of negatively charged dust grains on the plasma interaction. Figures 2a and 2b illustrate the scenario: the plasma, which flows in (+x) direction, undergoes collisions within a cylindrical volume (denoted by the black rectangle), leading to the generation of Alfvén wings, as illustrated by B_y. (a, c, e) The results without any dust and (b, d, f) the results with the cylindrical volume filled with a constant density of $\xi\ n_D = 2n_i/3$ (illustrated by the green area in Figure 2). Figures 2c–2f display a plane roughly perpendicular to the Alfvén wings (indicated by the black lines in Figures 2a and 2b). The circle of radius 3 R_E shows the approximate position of the Alfvén tube. Due to the small angle between the wings and the background magnetic field of about only arctan $M_A = 7°$ (also visible in Figures 2a and 2b), these currents are mainly given by j_z (compare Figures 2e and 2f). Without any dust, the Hall effect rotates these currents clockwise, while the dust-associated Anti-Hall effect causes a counter-clockwise rotation. This explains the different signs of the B_y component in Figures 2a–2d.

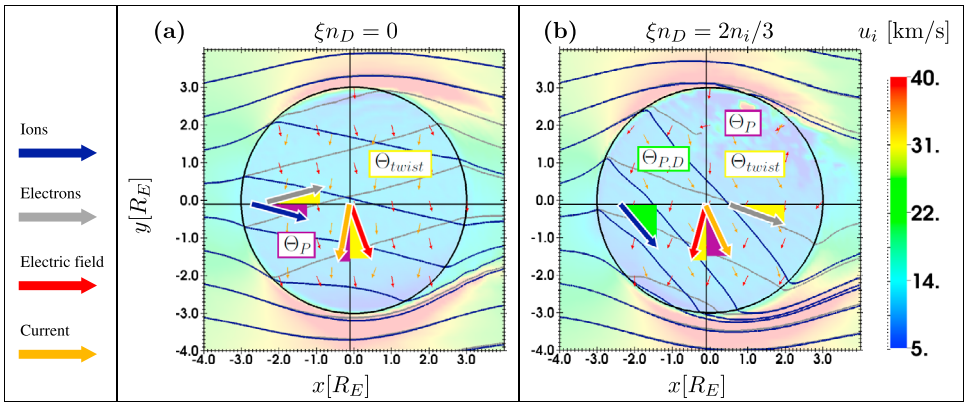

Figure 3. The directions of the electric field (red), the perpendicular current (orange), the electron velocity (given by $\underline{E} \times \underline{B}$, grey) and the ion velocity (blue) for the same uniform cylinder filled with neutral gas as discussed in Figure 2. We consider two different cases: no dust ($\xi n_D = 0$) and a uniform dust density of $\xi n_D = 2n_i/3$. Without dust, all quantities are twisted around the z axis due to the Hall effect [see also *Saur et al.*, 1999, Figure 9], while the electron absorption by dust (Figure 3b) yields an Anti-Hall effect, which reverses the directions of the twist of electron velocity, electric field and current due to the negative sign of the Hall conductivity. The ions, however, are deflected away from Saturn in both cases. The dust even enhances their deflection.

negative: south). Case 2 (ξn_D = 2/3 n_i) yields Σ_P = 14 S, Σ_H = −16 S and B_y = ∓9 nT. This is in good agreement with what can be obtained from Figure 2. For $\xi n_D = 0.2 n_i$ one gets Σ_H = 0 and therefore, a B_y perturbation of approximately zero (not shown here, but confirmed by simulation). Thus, we have shown that the reversal of the Hall current due to dust is not only an effect of the analytical, first-order perturbation theory applied by *Simon et al.* [2011], but can also be reproduced by our self-consistent simulation.

[43] *Simon et al.* [2011] only presented results for the magnetic field perturbations, while our model automatically also calculates currents and ion velocity. For a better understanding of the flow perturbations and currents associated with Hall and Anti-Hall effect, we compare our simulations with analytical results derived by *Saur et al.* [1999] for the same cylindrical geometry. For the electric field $\underline{E}$, the electron velocity $\underline{u_e}$ and the perpendicular current $\underline{j}_\perp$ inside the cylinder, Saur et al. derived

$$\underline{E} = \underline{E}_0 + E_P \begin{pmatrix} \sin\Theta_P \\ \cos\Theta_P \end{pmatrix}, \tag{13}$$

$$\underline{u_e} = u_e \begin{pmatrix} \cos\Theta_{twist} \\ \sin\Theta_{twist} \end{pmatrix}, \tag{14}$$

and

$$\underline{j}_\perp = -j_\perp \begin{pmatrix} \sin\Theta_P \\ \cos\Theta_P \end{pmatrix}, \tag{15}$$

where the angles are given by

$$\tan\Theta_P = \frac{2\Sigma_A\Sigma_H}{\Sigma_H^2 + \Sigma_P(\Sigma_P + 2\Sigma_A)} \tag{16}$$

and

$$\tan\Theta_{twist} = \frac{\Sigma_H}{\Sigma_P + 2\Sigma_A}, \tag{17}$$

respectively. Σ_A denotes the Alfvén conductance. Note that in the above expressions, the height-integrated conductivities have to be calculated from z = 0 to the top of the cylinder and therefore have half the values given earlier.

[44] All these equations are still valid when including dust in the cylinder. For the derivation of the ion velocity, however, *Saur et al.* [1999] used the explicit definition of Hall and Pedersen conductivities, depending on collision and gyration frequency. If the electron gyrofrequency clearly exceeds the effective electron collision frequency, the Hall conductivity is modified by the dust according to

$$\sigma_H = \frac{en_i}{B}\frac{\nu_{in}^2}{\nu_{in}^2 + \Omega_i^2} - \frac{e}{B}\xi n_D = \sigma_{Hi} - \frac{en_i}{B}k \tag{18}$$

(see equation (29) of *Simon et al.* [2011] with $k = \xi n_D/n_i$). Thus, we have to modify the expression for the ion velocity [*Saur et al.*, 1999, equation (A16)]. The symbol σ_{Hi} denotes the Hall conductivity in an electron-ion plasma without dust, the corresponding conductance is Σ_{Hi}. Analogous to *Saur et al.* [1999], we obtain for the ion velocity

$$\underline{u_i} = |\underline{u_i}| \begin{pmatrix} \cos\Theta_{P,D} \\ -\sin\Theta_{P,D} \end{pmatrix}, \tag{19}$$

with

$$\tan\Theta_{P,D} = \frac{2\Sigma_{Hi}\Sigma_A + k\Sigma_P\tilde{\Sigma}_{Hi}}{2\Sigma_A\Sigma_P + (1-k)\left(\Sigma_{Hi}^2 + \Sigma_P^2\right)}, \tag{20}$$

and the abbreviation

$$\tilde{\Sigma}_{Hi} \equiv \frac{\Sigma_{Hi}^2 + \Sigma_P^2}{\Sigma_{Hi}}. \tag{21}$$

One can easily verify that for $k \to 0$ also $\Theta_{P,D} \to \Theta_P$. To understand the implications of the above equations, Figure 3 shows our simulation results for the directions

of fields, currents and velocities in the (z = 0) plane. For case 1, i.e., without dust, our results are shown in Figure 3a. One can clearly see the deflection of electric field, electron velocity, current and ion velocity with the angles Θ_P and Θ_{twist}. From equations (16) and (17) we get $\Theta_{twist} \approx \Theta_P \approx 13°$, which is in good agreement with our simulation results.

[45] The situation gets different with dust. In an electron-ion plasma without dust, a vanishing Hall conductance $\Sigma_H \approx 0$ implies $\nu_{in} \approx 0$ and therefore no deflection of electric field, electron velocity, current and ion velocity. With dust, however, the modified quasi-neutrality condition ($n_i = n_e + \xi n_D$) yields $\Sigma_H \approx 0$, but $\Sigma_{Hi} \neq 0$ and therefore $\Theta_{PD} \neq 0$. Thus, what we can learn from equations (16), (17) and (20) is that only the ions should undergo a deflection. Physically this deflection is a result of the Pedersen current, where in the case of electrons attached to dust only the ions but not the charged dust particles move with respect to Enceladus.

[46] In case 2, the direction of rotation of electric field, current, and electron velocity reverses, since the Hall current reverses its sign. The ion flow, however, does not change its flow direction from $-y$ to $+y$, but the deflection away from Saturn gets even stronger, since it can be seen from equation (20) that $\Theta_{P,D} > \Theta_P$ for $k > 0$. This has the remarkable consequence that for the ions, the dust enhances the asymmetries, while for electrons, electric field and current the direction of rotation is reversed. The angles for case 2 are $\Theta_{twist} = -28°$, $\Theta_P = -20°$ and $\Theta_{P,D} = 54°$, which match well with Figure 3b.

5. Results for Selected Enceladus Flybys

[47] In section 4 we have shown that our hybrid model is in quantitative agreement with the analytical theory of Alfvén wing and Anti-Hall effect for a simplified test scenario. In this section, we are therefore going to discuss the effect of the negatively charged dust population on the plasma flow and magnetic field at Enceladus, i.e., for the realistic plume model and interaction scenario described in section 3.

[48] In order to understand the magnetic field measurements and model calculations along Cassini's 1D-trajectories, we present the results of our 3D simulations together with 1D comparisons between model and observations. We show that considering the electron absorption is necessary to quantitatively explain the observations. However, before we can understand the magnetic field structures, we have to consider the corresponding structures of plasma density and velocity.

[49] Since upstream and plume parameters are different for each flyby discussed here, we arbitrarily choose the E9 best fit case with an upstream density of $n_0 = 75$ cm^{-3} and a base density of $n_{n,0} = 6 \times 10^{10}$ cm^{-3} for all color plots shown in this section. The simulation including dust has an additional dust base density of $\xi n_{D,0} = 5.5 \times 10^2$ cm^{-3}.

5.1. Density and Velocity

[50] Figure 4 displays the densities of ions and charged dust in the (y = 0) and ($z = -4\ R_E$) planes. Figures 4b and 4e visualize the gas plume as the region where the ion density is enhanced due to the creation of new ions by electron impacts and photoionization (mass loading). Near the south pole, the ion density is about an order of magnitude larger than upstream. The slightly enhanced density downstream of the plume results from pick-up of the newly created ions [*Kriegel et al.*, 2009]. The dust charge density ξn_D (Figures 4c and 4e) has a maximum of $\xi n_D > 100$ cm^{-3} near the south pole and assumes a value of about $\xi n_D = 50$ cm^{-3} at $z = -4\ R_E$. Thus, the dropout in the electron density due to electron absorption by dust, which is required by our model to achieve agreement with MAG data (see sections 5.3–5.5), is on the order of 10% − −20% in the center of the plume. It is therefore possible to have a noteable difference in electron and ion densities while both are larger than the background density. This finding is in agreement with results from RPWS presented by [*Shafiq et al.*, 2011]. Since we can only provide dust charge densities, it is not easily possible to compare our results with dust measurements (for example by CDA). In order to relate our model densities of the *charged* dust to *number* densities, one would need to consider the number of electrons on grains of different sizes and the grain-size distribution of the dust which is by far out of the scope of this paper.

[51] Ion velocity and electric field are presented in Figures 4g–4i. In Figure 4g, one can see the deflection of the ion flow in ($-y$) direction (away from Saturn), as discussed in section 4. The twist of the electric field in ($-x$) direction in Figure 4h results from the Anti-Hall effect. As can be seen from Figures 4g and 4h, the pickup tail and the associated decrease in the electric field strength are essentially confined to the ($|y| < 1\ R_E$)-region, i.e., the tail exhibits a two-dimensional shape. This finding is in agreement with previous hybrid simulation results by *Kriegel et al.* [2009], who showed that the small gyroradii of the pick-up ions (on the order of 10 km) prevent the tail from a significant expansion in y direction. Within the plume, ion velocity and electric field decrease to approximately zero, in agreement with observations of flow stagnation by CAPS [*Tokar et al.*, 2009]. To further illustrate the effect of flow stagnation, Figure 4i displays the ion velocity in the ($z = -4\ R_E$) plane along the corotation axis (y = 0 line): the ion velocity decreases sharply below 1 km s^{-1} from $x = -1\ R_E$ to $x = 0.5\ R_E$, before it assumes a value of $u_i = 17$ km s^{-1} = 60% u_0 in the pick-up tail.

5.2. Magnetic Field: E5 and E6

[52] All Enceladus flybys in 2008 had trajectories basically in the (x, z) plane. For a better understanding of the perturbations visible in the MAG data, Figures 5a–5f show the results for the components of the magnetic field in that plane. For clarity, Figures 5a–5f only show the magnetic field perturbations (ΔB_x, ΔB_y, ΔB_z); the background field has been subtracted by fitting a dipole field. The black lines represent the projections of Cassini's trajectories during E5 and E6 on the (x, z) plane. Figures 5a–5c show the results for a pure gas plume without dust. In Figure 5a, the Alfvén wing can clearly be seen in the ΔB_x component. ΔB_y (Figure 5b) assumes positive and negative signs in both, the northern and the southern wing, which results from the clockwise rotation of the quadrupole-like structure of ΔB_y due to the Hall effect. The positive sign of ΔB_y in the center of the northern wing as well as the negative sign in the center of the southern wing are consistent with the results for the test scenario (see Figure 2). We would like to note

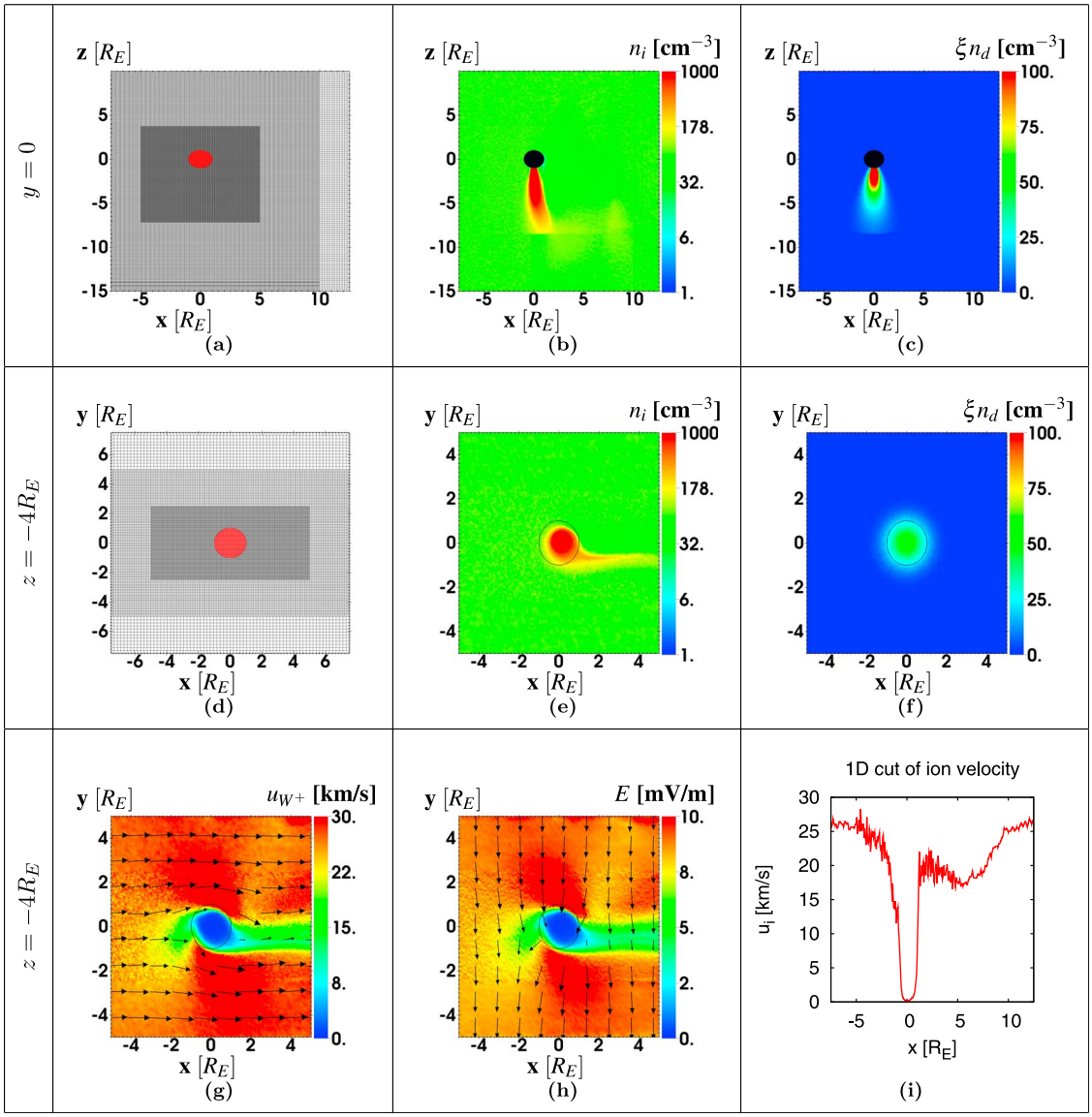

Figure 4. Simulation grid and dusty plasma near Enceladus: (a and d) the simulation mesh with the different levels of refinement. (b and e) The ion number density, which is enhanced in the plume by about an order of magnitude due to electron impact and photoionization. (c and f) The dust charge density is comparable to the upstream plasma density. (g–i) Ion velocity and electric field along the $y = 0$ line and in two dimensions. The ion velocity decreases to stagnation within the plume.

that an ideal MHD model (i.e., without Hall effect) would yield $\Delta B_y \approx 0$ at $y = 0$. The ΔB_z component in Figure 5c assumes a negative value in the magnetic pile-up region in front of the plume and a positive value at the downstream side (since it is $B_z < 0$ for the background field). These structures have already been described in detail in our previous study [*Kriegel et al.*, 2009] as well as by *Jia et al.* [2010c].

[53] Figures 5d–5f show the results of a simulation with dust included. As expected, the ΔB_y component inside the Alfvén flux tube has reversed its sign. On the other hand, no modification of ΔB_x is visible. Note that the condition for the occurrence of the Anti-Hall effect (inequality (3)) is not fulfilled in the center of the plume, since there, the ion density n_i strongly exceeds the dust charge density ξn_D (see Figure 4) and the ion-neutral collision frequency ν_{in} is larger than the ion gyro frequency Ω_i. In the outer regions of the plume, however, ion and neutral density decrease stronger than the dust charge density, which allows inequality (3) to be fulfilled. Since the Alfvén wings are determined by the height-integrated conductivities Σ_H and Σ_P, the sign of Σ_H (and ΔB_y) reverses, although in the center of the plume the local Hall conductivity σ_H assumes a positive value. This is an à posteriori justification of our difference in the models of the neutral gas and the charged dust, since only the weaker radial decrease and the larger opening angle of the dust plume allow us fulfill inequality (3) in the outer regions of the plume. The most important result, especially with

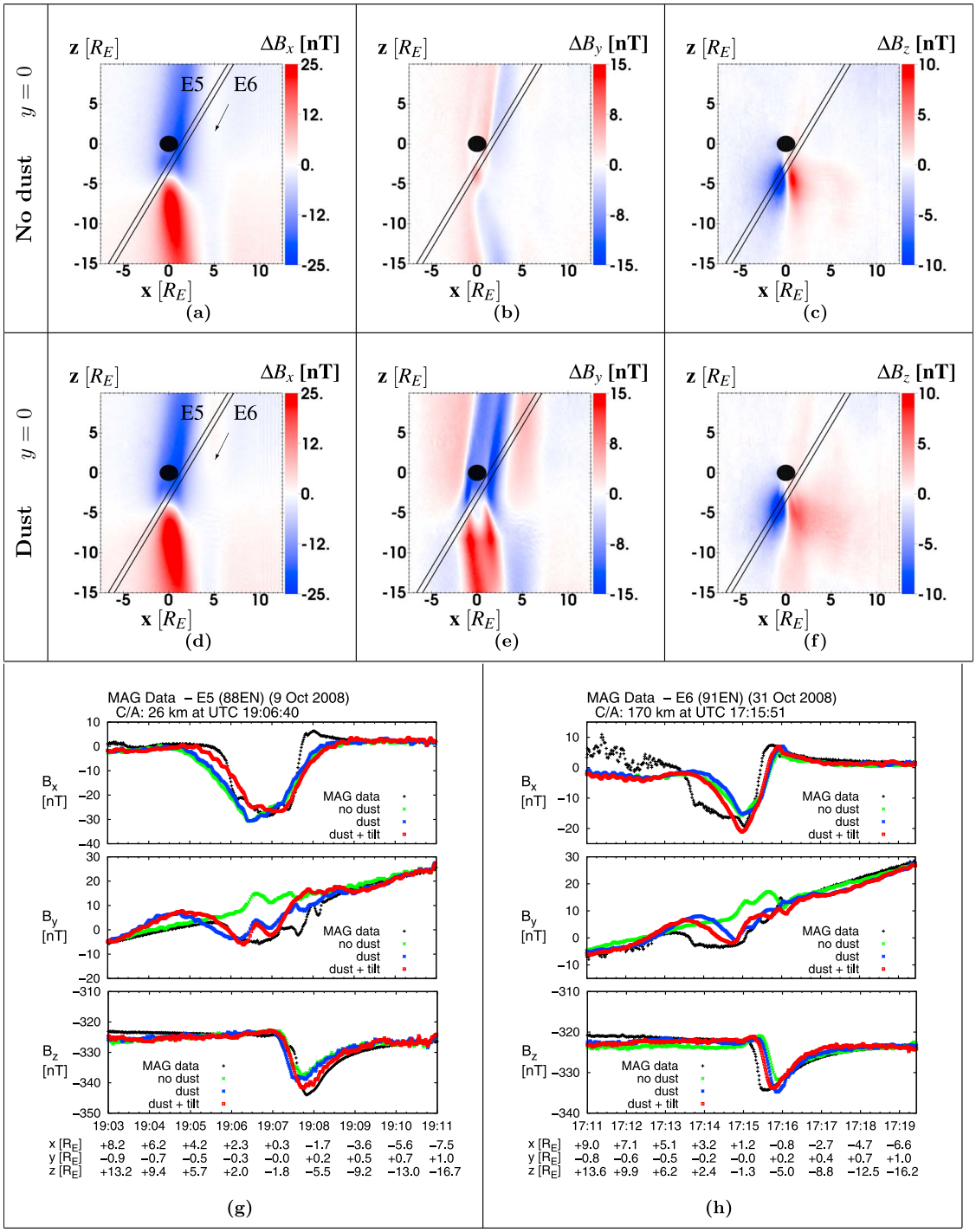

Figure 5. (a–f) Simulated magnetic field components in the (x, z) plane together with the trajectories of E5 and E6. Figures 5a–5c display the results without dust, while Figures 5d–5f show the reversal of the B_y component when the presence of the negatively charged dust is considered. (g and h) A comparison of simulation results with Cassini MAG data (black) for E5 (Figure 5g) and E6 (Figure 5h) for a simulation without dust (green), with dust (blue) and the best fit including dust and a tilted plume (red).

respect to the work of *Simon et al.* [2011], is that the reversal of ΔB_y due to electron absorption by dust also occurs for a more realistic, inhomogeneous plume model.

[54] We would also like to point out that our results show that the northern wing (negative ΔB_x) does not begin at Enceladus' south pole, but about 2 R_E below. Thus, our simulation confirms that the draping or momentum loading center is shifted about 2 R_E downward from the south pole, in agreement with the findings of *Khurana et al.* [2007] for E0–E2. It is remarkable that our simulation succeeds in reproducing this aspect of the interaction without reducing the neutral density near the south pole to account for a

Table 2. Upstream Density n_0 (From RPWS Electron Densities) and Best Fit Parameters for Each Flyby[a]

Flyby	Date	n_0 (cm^{-3})	$n_{n,0}$ (cm^{-3})	$\xi n_{D,0}$ (cm^{-3})	Lat	Lon (West)
E5	9 Oct 2008	90	11×10^{10}	8.5×10^2	−85°	270°
E6	31 Oct 2008	45	7×10^{10}	5.5×10^2	−85°	90°
E7	2 Nov 2009	60	7×10^{10}	5.5×10^2	–	–
E8	21 Nov 2009	45	2×10^{10}	2.0×10^2	−80°	67.5°
E9	28 Apr 2009	75	6×10^{10}	5.5×10^2	–	–
E11	13 Aug 2010	60	5×10^{10}	4.0×10^2	–	–

[a] $n_{n,0}$ and $\xi n_{D,0}$ denote the base densities of neutral H_2O molecules and charged dust, respectively. Some flybys (E5, E6, E8) match better with the data when a tilt of the plume is considered. The plume is then centered at the respective planetographic latitudes (Lat) and longitudes (Lon) on Enceladus' surface.

reduced ionization efficiency in that region, as proposed by *Jia et al.* [2010c]. By comparing the ΔB_z components in Figures 5c and 5f, one can see that the magnetic cavity region is shifted downward, if dust is considered.

[55] A quantitative comparison between MAG data from E5 and E6 and simulation results is provided in Figures 5g and 5h. MAG data are black, and the colors indicate different simulation setups: no dust (green), with dust (blue) and the best fit with dust and a tilted plume (red). By comparison of the observations from both flybys it is evident that the perturbation is stronger for E5 (up to 30 nT) than for E6 (less than 20 nT) [see also *Jia et al.*, 2010a]. This might not only be an effect of a variable plume activity, but also of the different upstream densities for these flybys: for strong perturbations (as the observed flow stagnation) and a symmetric interaction geometry, the bending of the magnetic field lines is identical to the inclination of the Alfvén wing ($M_A = \tan \Theta_A \cong \Delta B_x/B_0$) [*Neubauer*, 1980], which yields

$$\Delta B_x \cong M_A B_0 \sim \sqrt{n_0}. \tag{22}$$

Thus, a higher upstream density yields a stronger perturbation. For E5 and E6, the densities were $n_0 = 90$ cm^{-3} and $n_0 = 45$ cm^{-3}, respectively [*Jia et al.*, 2010b]. Based on the densities alone, one would expect the B_x perturbation during E5 to be about a factor of $\sqrt{2}$ stronger than during E6, which matches well with the observed field perturbation (30 nT/20 nT = 1.5 ≈ $\sqrt{2}$). However, in order to reproduce the strength of the measured perturbations (in particular ΔB_x), different source strengths of the plume of $n_{n,0} = 1 \times 10^{11}$ cm^{-3} (E5) and $n_{n,0} = 7 \times 10^{10}$ cm^{-3} (E6) were required. Thus, the stronger perturbation measured during E5 is not only an effect of the higher upstream density as suggested by equation (22), but also of a stronger plume activity by a factor of 1.5. This also implies that equation (22) is not strictly applicable. The reason is that the wing-aligned currents flowing toward Saturn's northern hemisphere are partially blocked by the solid body of Enceladus [*Saur et al.*, 2007]. According to equation (12), the plume densities correspond to production rates of about $Q = 3.7 \times 10^{29}$ H_2O s^{-1} (E5) and $Q = 2.4 \times 10^{29}$ H_2O s^{-1} (E6). The absolute values are about an order of magnitude larger than those derived by other authors [*Saur et al.*, 2008; *Omidi et al.*, 2010; *Jia et al.*, 2010b]. This mainly results from our narrow plume, since for a larger opening angle (e.g., $H_\vartheta = 15°$), equation (12) yields a production rate that is an order of magnitude lower for the same neutral base density. A summary of the best fit parameters is given in Table 2.

[56] Data from both flybys (black) show a steep decrease of the B_x component at the downstream side ($x > 0$, inbound), which is not seen in the simulation results (in particular for E6). This has also been found by *Simon et al.* [2011]. Both models have in common that they assume the collision frequency to be the same upstream and downstream. However, in reality the ion composition and therefore also reaction rate and collision frequency vary due to changes in the ion composition when moving through the plume from upstream to downstream. This is confirmed by the fact that downstream mainly H_3O^+ is present [*Cravens et al.*, 2009]. Thus, this discrepancy could be due to the rough description of the ion-neutral chemistry in these two models. Including a more sophisticated model of the chemistry will be subject to future studies. At the upstream side ($x < 0$, outbound), the simulations reproduce the sharp increase in B_x during E6, while it is smoother for E5. This can also be seen in Figure 5d, where the upper trajectory (E5) passes through a region of negative ΔB_x upstream of the plume. In contrast, the lower trajectory (E6) passes along the uppermost end of the southern wing (positive ΔB_x).

[57] Figures 5a–5f also show that the dust does not have any influence on the B_x and B_z components along E5 and E6 when comparing the simulations with (blue) and without dust (green). In the B_y component, it can be seen that the dust not only qualitatively reverses the sign of ΔB_y but also quantitatively explains the magnitude of the measured B_y perturbation. The base densities of the charged dust particles in the simulations are $\xi n_{D,0} = 8.5 \times 10^2$ cm^{-3} for E5 and $\xi n_{D,0} = 5.5 \times 10^2$ cm^{-3} for E6. The variation of the dust base densities is about a factor 1.5, and therefore, the variability of gas and dust plume is the same. However, for both flybys our simulations are not able to reproduce the extension widths of the B_y perturbation: for E5, our modeled B_y only matches the location of the decrease (downstream), while for E6, only the position of the increase to the background value in the upstream region is reproduced. This may result from a larger extend of the dust plume near the surface. Furthermore, in Figure 5e it appears as if the trajectories pass through the southern Alfvén wing with $\Delta B_y > 0$, while the 1D comparisons only exhibit negative B_y perturbations. This striking difference only results from Cassini's motion in y direction and can be understood when the 3D geometry of the flyby is taken into account: upstream of the plume ($x < 0$), Cassini is located at $y > 0$. There, the B_y perturbation is negative, while it is positive along the projection on $y = 0$.

[58] For B_z, simulations and data match very well. As the modeled perturbation in the B_z component is negative along

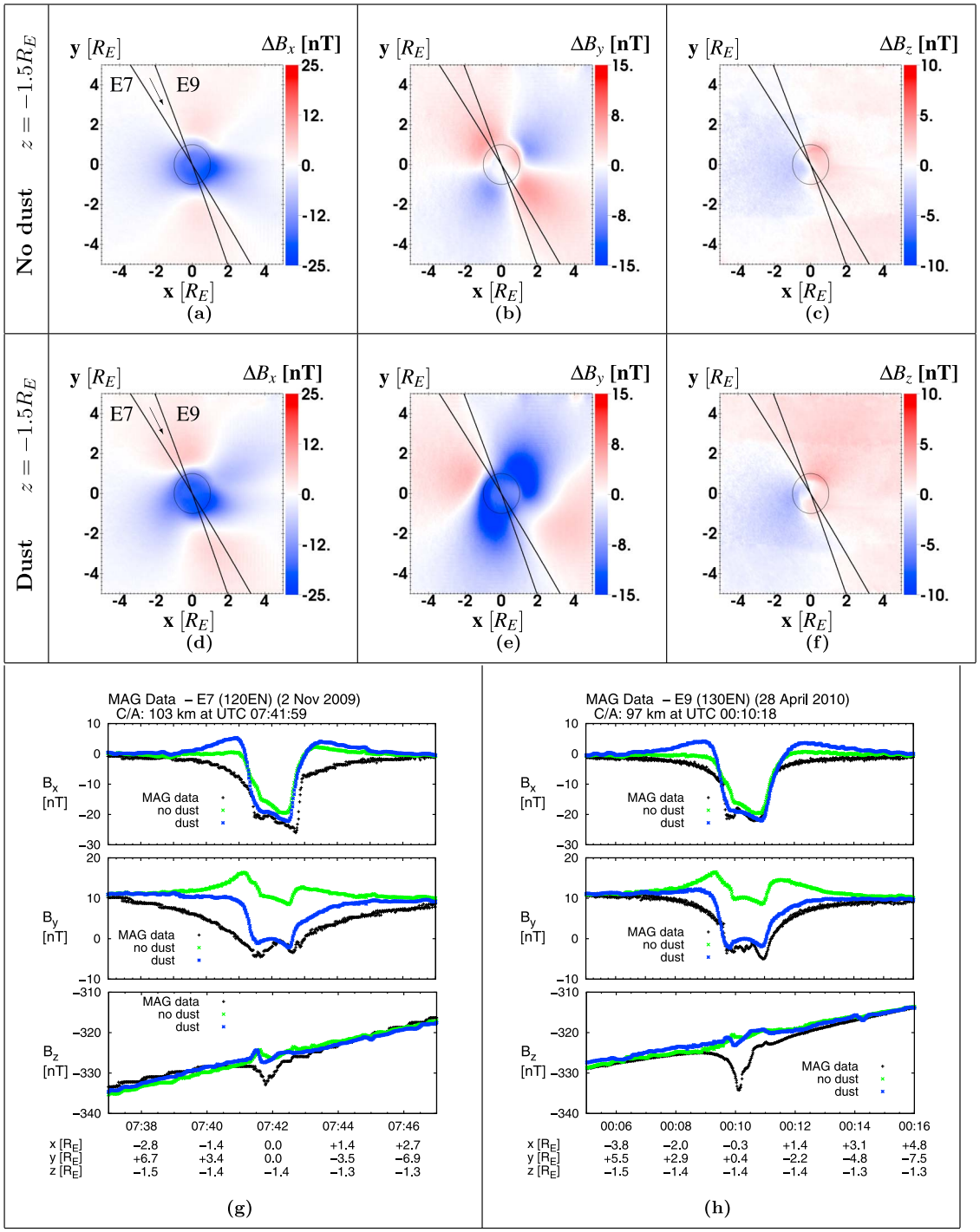

Figure 6. Simulated magnetic field components in the ($z = -1.5\ R_E$) plane together with the projected trajectories of E7 and E9 (Figures 6a–6f). (a–c) the results without dust and (d–f) the counter-clockwise rotation of the magnetic field structures due to the Anti-Hall effect when electron absorption by dust is considered. (g and h) A comparison of simulation results with Cassini MAG data (black) for E7 (Figure 6g) and E9 (Figure 6h) for a simulation without (green) and with dust (blue).

the entire trajectories, our simulations are also successful in reproducing that Cassini only penetrated through the magnetic pile-up region, but did not intersect the magnetic cavity. The location of the flyby trajectories with respect to the magnetic pile-up region and cavity is also illustrated in Figure 5f. For E5, our simulations do not show any further dips before or during the main perturbations around 19:07:20 UTC in B_x and B_z in contrast to the data. A reason for this might be that the trajectory of E5 was so close to the south pole (C/A distance of only 25 km) that these structures are caused by single jets which are not resolved by our plume model.

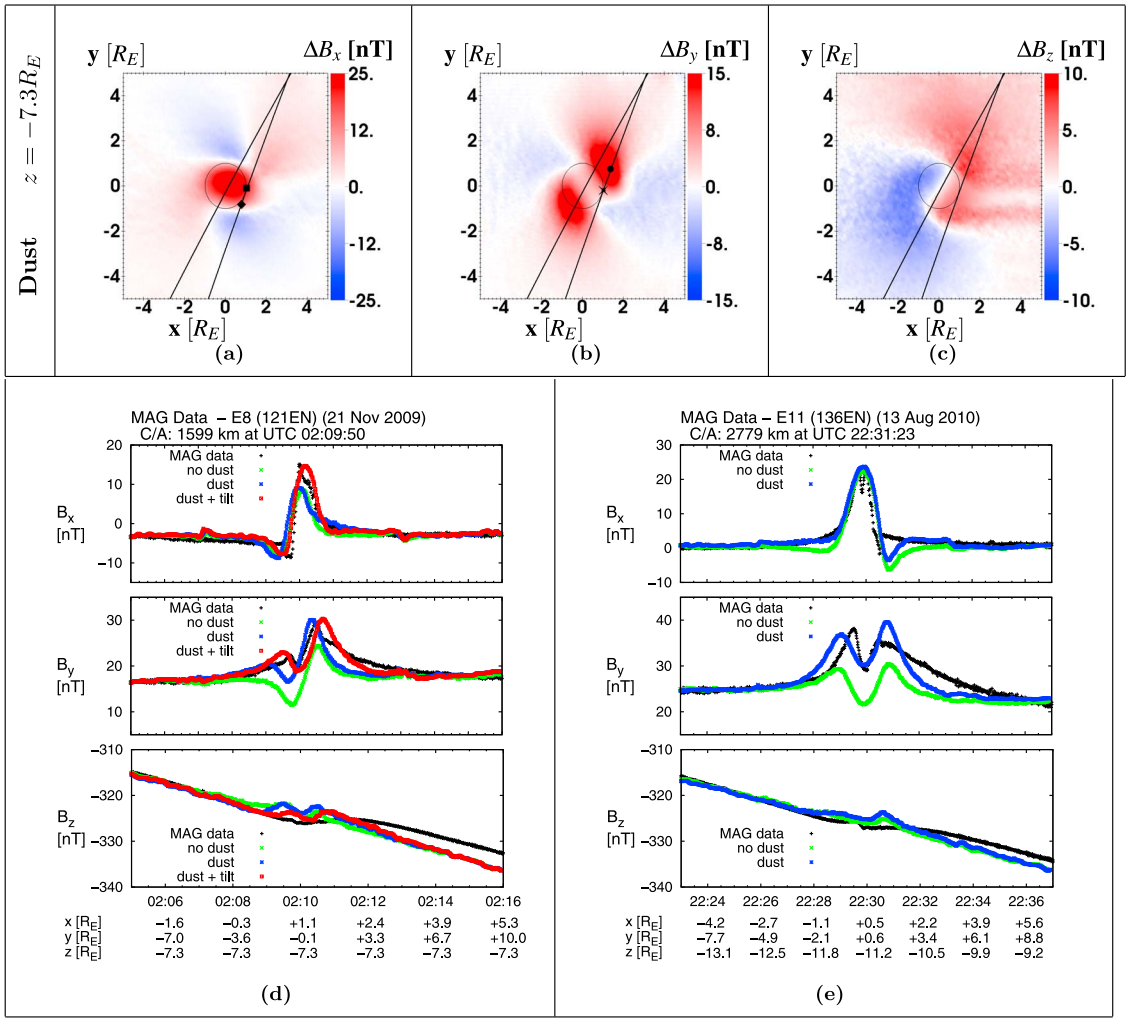

Figure 7. Simulated magnetic field components in the ($z = -7.3\ R_E$)-plane together with the projected trajectories of E8 and E11 (Figures 7a–7c). The symbols mark the positions of features visible in the data. (d and e) A comparison of simulation results with Cassini MAG data (black) for E8 (Figure 7d) and E11 (Figure 7e) for a simulation without dust (green), with dust (blue) and the best fit including dust and a tilted plume (red, only E8).

[59] The red curves show that for both flybys, a tilt of the plume improves the agreement between data and simulation. In particular, the positions of the outbound flank of the region with reduced B_x, the entry into the pile-up region in B_z and its magnitude match observations better when introducing a tilt of the plume. However, the tilt applied for E5 (Lat = −85°, Lon = 270°, upstream) has the opposite direction as for E6 (Lat = −85°, Lon = 90°, downstream). These different tilts correspond to different plume activities. We therefore propose that during E5, other and possibly stronger jets were active than during E6. For a further investigation of this finding, a multijet gas and dust plume model within a plasma simulation is required.

5.3. Magnetic Field: E7 and E9

[60] The second group of flybys on which we focus are E7 and E9. The upstream densities are $n_0 = 60\ \mathrm{cm}^{-3}$ for E7 and $n_0 = 75\ \mathrm{cm}^{-3}$ for E9. Figure 6 displays the components of the magnetic field perturbation in the plane of these flybys ($z = -1.5\ R_E$) together with the flyby trajectories. Analogous to Figure 5, Figures 6a–6c display the results without dust, while dust is included in the results shown in Figures 6d–6f. In ΔB_x and ΔB_y, the Alfvénic structures caused by the wing-aligned currents are clearly visible: within the northern Alfvén flux tube, ΔB_x is negative. At the flanks at about $y = \pm R_E$, ΔB_x sharply assumes a small positive value, while along the x-axis, it smoothly gets to zero. Again our simulation therefore confirms that the draping center is located below $z = -1.5\ R_E$. ΔB_y exhibits a quadrupole-like structure, slightly rotated around the z axis due to Hall or Anti-Hall effect. As discussed in section 4, the direction of this rotation depends on the sign of Σ_H: clockwise without dust and counter-clockwise for the Anti-Hall effect. When comparing the ΔB_y component of the simulations with and without dust (Figures 6e and 6b), it is also evident that the symmetric quadrupole-like structure is stretched in y direction by the influence of the dust, yielding a larger region with negative ΔB_y (compare Figure 6e). In B_z, the magnitude of the perturbation is less than 5 nT = 1.5%B_0 in this plane. This is because the strongest magnetic pile-up is

located ahead of the momentum loading center, which can be found south of this plane (see also Figure 5). Moreover, Figure 6f shows that pile-up and cavity region are also twisted by the Anti-Hall effect, such that the two flybys did not pass through the center of either of them.

[61] The comparison between data and simulations is shown in Figures 6g and 6h. Again, MAG data are colored in black, the other colors indicate different simulation setups: no dust (green) and the best fit with dust (blue). We achieve very good agreement for the perturbations in B_x. The magnitude and the sharpness of the jumps in B_x match exactly for both flybys. It is ΔB_x = 20–25 nT for E7 and $\Delta B_x \sim 20$ nT for E9. Since the upstream density is smaller, but the perturbation is stronger for E7 than for E9, we expect the plume activity to be slightly stronger for E7 according to the discussion in section 5.2. This is confirmed by our results: in order to reproduce the strength of the B_x perturbation, a neutral base density of $n_{n,0} = 7 \times 10^{10}$ cm^{-3} and $n_{n,0} = 6 \times 10^{10}$ cm^{-3} was required for E7 and E9, respectively. The corresponding production rates are $Q = 2.4 \times 10^{29}$ H_2O s^{-1} (E7) and $Q = 2.1 \times 10^{29}$ H_2O s^{-1} (E9). Therefore, the variability of the plume activity between E7 and E9 of about a factor of 1.2 is smaller than between E5 and E6 (factor 1.5). The strong positive spikes seen by the model of *Simon et al.* [2011] inbound and outbound of the Alfvénic flux tube are only weak in our simulation results (<5 nT versus >10 nT). Therefore, these spikes can be regarded an effect of the simplified plume model used by Simon et al., which concentrates the field-aligned currents on the surface of a cylindrical plume.

[62] Again, the B_y perturbation clearly shows the effect of the electron-absorbing dust on the outcome of the simulation (blue), compared to a scenario without dust (green). Without dust, the sign of the B_y perturbation in our simulation is completely different from the observations, while we achieve very good agreement with the data when dust is included. The base densities of the charged dust particles in the simulations are $\xi n_{D,0} = 5.5 \times 10^2$ cm^{-3} for E7 and $\xi n_{D,0} = 5.5 \times 10^2$ cm^{-3} for E9. Therefore, our simulations reveal no change in the activity of the dust plume from E7 to E9, in agreement with the small variability in the gaseous part of the plume. The smooth increase to zero in the B_y component for $y < 0$ during E9 is in good agreement with MAG data, while the simulations (blue) show a sharper decrease for $y > 0$ than the data (in particular for E7). We suppose this to be due to the geometry of our dust plume, since in reality most dust particles fall back onto the surface, leading to a wider plume close to the moon [*Kempf et al.*, 2010].

[63] Despite the good agreement in B_x and B_y, our simulation is not able to reproduce the observed small pile-up in B_z. In our simulations (blue, green), Cassini only passed at the edge of the cavity region (positive ΔB_z), without intersecting the region of enhanced $|B_z|$. The stair-case in the observed B_z for E7 is due to a range switch of the instrument. We do not present a best fit simulation with a tilted plume here, since any tilt we tested did not yield a substantial improvement of the fit.

5.4. Magnetic Field: E8 and E11

[64] The last pair of flybys that we discuss in this paper is E8 and E11. Both occurred far below the moon's orbital plane. So far, E8 and E11 are the only flybys which intersected the southern Alfvén wing. Since the trajectory of E8 was nearly parallel to the equatorial plane at $z = -7.3$ R_E, we show our 2D results in that plane in Figure 7. The black lines indicate the projected trajectories of E8 and E11, the symbols mark the positions of features visible in the data. The magnetic field perturbations in the southern Alfvén wing (ΔB_x and ΔB_y) reveal the same structures as seen in Figure 6 for the northern Alfvén wing (when including dust), but with opposite signs: ΔB_x is positive inside the flux tube and negative at the flanks at $y = \pm R_E$. In addition, ΔB_x assumes small positive values in the (x, $y > 0$) region and decreases with increasing distance to the Alfvén flux tube. In ΔB_y, the positive perturbation is stretched in y direction. The B_z perturbation in Figure 7c is similar to Figure 6f, but the magnitude of ΔB_z at $z = -7.3$ R_E is a little stronger than at $z = -1.5$ R_E (≈5 nT compared to ≈2 nT). This means that the location of pile-up region and cavity does not change when moving from $z = -1.5$ R_E (E7, E9) to $z = -7.3$ R_E along the z axis. We do not show 2D results for the simulation without dust, as Figure 6 contains no new information.

[65] The comparison between data and simulations for E8 is shown in Figure 7d. Similar to Figures 5 and 6, MAG data are black, and the three simulation setups are as follows: without dust (green), with dust (blue), best fit with dust and a tilted plume (red). The measured B_x component shows a narrow and sharp decrease from −4 nT to −8 nT at about $(0.8, -0.9, -7.3)R_E$ (02:09:32 UTC, diamond in Figure 7a), which occurs within 30 km centered around $(x - M_A|z|)^2 + y^2 = R_E^2$, that is around the Enceladus flux tube [*Simon et al.*, 2011]. Such a discontinuity-like jump in the magnetic field is likely caused by a very confined or even surface current tangential to the body of Enceladus. This current is supposed to be part of the hemisphere-coupling current system proposed by *Saur et al.* [2007], which arises from the partial blockage of the Alfvénic currents by the body of the moon. As a northward current, it produces auroral hiss observed by the Cassini Radio and Plasma Wave Science (RPWS) instrument [*Gurnett et al.*, 2011]. The subsequent increase of the B_x component to a sharply peaked maximum of 15 nT at $(1.1, -0.1, -7.3)R_E$ (rectangle in Figure 7a) and the following decrease are associated with nearly field-aligned southward and northward Alfvénic currents. The latter could also in principle contribute to the southward field-aligned electron beams generating auroral hiss. An outbound southward hemisphere coupling current cannot be distinguished from the Alfvénic current in the magnetic field data. It would also be invisible in the hiss observation because of the wrong electron beam direction.

[66] Both, the simulation with (blue) and without dust (green) succeed in reproducing the structure of the perturbation as well as the magnitude of the positive peak, while the magnitude of the negative B_x perturbation in our simulation is stronger than measured. Furthermore, in our simulation the B_x perturbation starts earlier, that is at smaller y than observed by Cassini. This can also been seen in Figure 7a, where the diamond is located above the edge of the negative ΔB_x. The measured B_y perturbation during E8 shows a steady increase to a maximum of 29 nT at $(1.4,0.8, -7.3)R_E$ (02:10:31 UTC, circle in Figure 7b), which is interrupted by a small negative dip of 3 nT at $(1.0, -0.2, -7.3)R_E$ (02:09:58 UTC, cross in

Figure 7b). By comparing with Figure 7b, these structures can be explained as follows: inbound, Cassini passed through the outer positive part of the warped quadrupole-like B_y structure, where the perturbation increased as the spacecraft approached the flux tube. At (1.0, −0.2, −7.3)R_E (cross in Figure 7b), Cassini was located at the edge of the flux tube where the negative part of the warped quadrupole-structure begins. Thus, B_y decreases, before the spacecraft enters the opposite region of positive B_y. This has already been described by *Simon et al.* [2011]. These structures are different in our simulation without dust (green), since the direction of rotation as well as the stretching of the quadrupole-like B_y is not seen without dust (see Figure 6b). With dust (blue), our simulation reveals a similar structure as visible in the data. Similar to B_x, the location of the perturbation is slightly displaced.

[67] The simulation with dust and a tilted plume (red) shows that the locations of the features in B_x and B_y match better with the data when the plume is tilted downstream and a little toward Saturn, i.e., the plume center is located at Lat = −80° and Lon = 67.5°. The base densities used to reproduce the magnitude of the perturbations measured during E8 are $n_{n,0} = 2 \times 10^{10}$ cm^{-3} and $\xi\, n_{D,0} = 2.0 \times 10^2$ cm^{-3}.

[68] For the B_z component, the data show a small decrease of 3 nT around (1.1, −0.1, −7.3)R_E (02:10 UTC), which means that even 1 R_E downstream, $|\underline{B}|$ is enhanced. This is neither expected nor reproduced by our simulations, since any magnetic pile-up is thought to occur at the upstream side of the plume. As mentioned above, we think that the measured locations of pile-up and cavity region might be reproduced when considering the different reaction rates of the water group ions.

[69] For the E11 encounter, the comparison between data and simulations is shown in Figure 7f. MAG data from E11 have already been presented by *Gurnett et al.* [2011] within the context of auroral hiss observations. Since any tilt of the plume yielded no better match with the data, we only show the results for simulations without (green) and with dust (blue). The observed B_x component (black) shows a strong but steady increase with a sharp dip of −7 nT at (0.4, 0.4, −11.3)R_E near the maximum perturbation of 23 nT. In the outbound region at (1.0, 1.4, −11.3)R_E another sharp dip to a minimum value of −1 nT was observed, before B_x returns to its background value. Since the trajectory of E11 is located about 1 R_E upstream of E8 in the interval considered here, Cassini did not pass through the region of negative ΔB_x inbound, but outbound (see Figure 7a). Similar to the inbound increase during E8, the outbound decrease by 18 nT during E11 is located in a region of 90 km centered around $(x - M_A|z|)^2 + y^2 = R_E^2$. Again we suppose this to be caused by the hemisphere-coupling surface currents. The steep flanks of the major peak in B_x are well reproduced by both simulation setups. However, the sharp dip at the top of the enhancement is not seen in our high-resolution simulations. The outbound dip is reproduced by our simulations, but appears much broader and deeper.

[70] B_y exhibits a similar structure as B_x, but the dip imposed on the maximum perturbation of 15 nT is broadened to an "M"-like structure and is with −8 nT also deeper than in the data. The outbound dip in B_x is located at the same position as the second maximum (14 nT) of the M in B_y (i.e., (1.0, 1.4, −11.3)R_E at 22:30:30 UTC). Without dust (green), our results reveal a similar M-like pattern, but centered around $\Delta B_y = 0$ nT, whereas the simulation with dust (blue) matches well with the data.

[71] In the B_z component, MAG data show a small bipolar signature of 1 nT magnitude at (0.3, 0.3, −11.3)R_E (22:29:44 UTC), while in our simulations, Cassini passes through a region with reduced magnetic field of 2 nT according to Figure 7c.

[72] The base densities used to match the magnitude of the perturbations measured during E11 are $n_{n,0} = 5 \times 10^{10}$ cm^{-3} and $\xi n_{D,0} = 4.0 \times 10^2$ cm^{-3}. Thus, gas and dust plume seem to have been between a factor of 2–3 times more active during E11 than during E8. Similar as for E7 and E9, any tilt of the plume yielded no improvement of the fit.

5.5. Variability of the Plume

[73] Table 2 summarizes the parameters used for the best fit simulations presented in sections 5.1–5.4. We would like to point out that we do not intend to provide *absolute* numbers for the neutral density or amount of dust in reality. That would require a more sophisticated model of the plume. Based on our results, we can instead analyze the *relative* variations of the gas production rate between the flybys studied in this paper and use the absolute numbers only as an estimate for the order of magnitude of these quantities.

[74] We find that the variability of the gas production rate lies within a factor of two (with E5 having the strongest and E8 the weakest plume activity). During all analyzed pairs of similar flybys, gas and dust plume have a similar variability: a factor of about 1.5 between E5 and E6 as well as a factor of 2–3 for E8 and E11 and an even smaller variation when comparing E7 and E9. Between E5 and E8, the activity even varies by a factor of five. However, the degree to which the results are affected by our model assumptions may differ between flybys of different geometry. Therefore, we only would like to underline the variability between similar flybys by a factor of 2 or less, but not the variability between all flybys.

[75] This variability of the plume intensity is consistent with the different tilts which improved the agreement between MAG data and simulations for some of the flybys (E5, E6, E8). Any tilt of our single-plume model means that different jets or active regions contribute to the plume. If we assume that the jets have a small inclination against the surface normal, our results imply a stronger activity of the "Damascus" tiger stripe for E5, while during E6 "Alexandria" was more active. For E8, our simulations reveal a tilt direction similar to E6, but even stronger.

[76] We would like to close this section with a cautionary remark: our model includes a high number of parameters ($n_{n,0}$, N_D, H_ϑ, H_d, ϑ_0, φ_0) which characterize the plume, while our results show that the measured magnetic field signatures are strongly affected by even minor changes in the plume geometry. We therefore cannot rule out the possibility that there are other sets of parameters which also explain the observed magnetic field perturbations or that a multiplume model is able to match the data for all flybys without using different jets and tilts.

6. Summary

[77] In the present study, we have applied the hybrid simulation code AIKEF to the plasma interaction of Enceladus.

We extended our previous model [*Kriegel et al.*, 2009] such that we do not only describe mass loading via photoionization and electron impacts but also momentum loading due to charge exchange. By using an analytical model, *Simon et al.* [2011] recently showed that electron absorption by dust grains may yield a reversal of the sign of the Hall conductivity (Anti-Hall effect), thereby changing the sign of the B_y component in Enceladus' Alfvén wings. This effect has been observed during all Enceladus flybys so far. The second major improvement therefore was the inclusion of a negatively charged dust population in the hybrid model.

[78] The purpose of this study was to analyze the influence of electron absorption by dust on the structure of Enceladus' Alfvén wings. In the first part, the Anti-Hall effect in the hybrid model was analyzed for a simple test scenario with a cylindrical, homogeneous obstacle, for which our results could be compared to analytical calculations of *Saur et al.* [1999]. In the second part, we compared our simulation results against Cassini MAG data for selected pairs of similar Enceladus flybys: (E5, E6), (E7, E9) and (E8, E11).

[79] Our main results are as follows:

[80] 1. The hybrid simulations confirm that electron absorption by dust reverses the Hall current (Anti-Hall effect). This implies a change in the sign of the magnetic B_y perturbation, which is quantitatively reproduced by our simulations for a simplified test scenario.

[81] 2. The deflection of the magnetospheric ion flow in the anti-Saturnward direction within the neutral gas cloud is enhanced by the presence of dust. In contrast to that, the direction of rotation reverses for electric field, electron flow and perpendicularcurrent. The resulting directions are in quantitative agreement with analytical theory.

[82] 3. Within the plume, the ion flow is slowed down below 1 km s^{-1}.

[83] 4. Our results are in good quantitative agreement with MAG data for all flybys studied in this paper (E5–E9 and E11).

[84] 5. The hemisphere-coupling current system proposed by *Saur et al.* [2007] and found to be present in MAG data by *Simon et al.* [2011] is also evident in our simulation results.

[85] 6. We find a small variability in the activity of the plume during all analyzed pairs of similar flybys by about a factor of two.

[86] 7. For some flybys (E5, E6 and E8) simulations and MAG data match better if a (different) tilt of the plume is considered.

[87] For a further interpretation of magnetic field data obtained near Enceladus as well as for a meaningful comparison of our results with data from other instruments, it will be necessary to include a more detailed model of the ion-neutral chemistry in the plume. Moreover, the analysis of data from above Enceladus' north pole obtained during the E12 and E13 encounters will require a sophisticated (multijet) plume model for gas and dust.

[88] **Acknowledgments.** H.K. and U.M. acknowledge financial support by the Deutsche Forschungsgemeinschaft (DFG) under grant MO539/18-1 (Special Program SPP1488, PlanetMag). The authors are grateful to Alexandre Wennmacher (University of Cologne) for processing of Cassini Magnetometer data. H. K. and S.S. acknowledge the valuable help of Bastian Koertgen (University of Cologne) with the final simulation runs. The simulations were performed on the systems of the North-German Supercomputing Alliance (HLRN).

[89] Masaki Fujimoto thanks the reviewers for their assistance in evaluating this paper.

References

Bagdonat, T. (2004), Hybrid simulation of weak comets, Ph.D. thesis, TU Braunschweig, Braunschweig, Germany.

Bagdonat, T., and U. Motschmann (2002), From a weak to a strong comet—3D global hybrid simulation studies, *Earth Moon Planets*, *90*, 305–321, doi:10.1023/A:1021578232282.

Bößwetter, A., T. Bagdonat, U. Motschmann, and K. Sauer (2004), Plasma boundaries at Mars: A 3-D simulation study, *Ann. Geophys.*, *22*(12), 4363–4379, doi:10.5194/angeo-22-4363-2004.

Burger, M. H., E. C. Sittler, R. E. Johnson, H. T. Smith, O. J. Tucker, and V. I. Shematovich (2007), Understanding the escape of water from Enceladus, *J. Geophys. Res.*, *112*, A06219, doi:10.1029/2006JA012086.

Cravens, T. E., R. L. McNutt, J. H. Waite, I. P. Robertson, J. G. Luhmann, W. Kasprzak, and W.-H. Ip (2009), Plume ionosphere of Enceladus as seen by the Cassini ion and neutral mass spectrometer, *Geophys. Res. Lett.*, *36*, L08106, doi:10.1029/2009GL037811.

Dougherty, M. K., K. K. Khurana, F. M. Neubauer, C. T. Russell, J. Saur, J. S. Leisner, and M. E. Burton (2006), Identification of a dynamic atmosphere at Enceladus with the Cassini Magnetometer, *Science*, *311*, 1406–1409, doi:10.1126/science.1120985.

Farrell, W. M., W. S. Kurth, D. A. Gurnett, R. E. Johnson, M. L. Kaiser, J. Wahlund, and J. H. Waite (2009), Electron density dropout near Enceladus in the context of water-vapor and water-ice, *Geophys. Res. Lett.*, *36*, L10203, doi:10.1029/2008GL037108.

Farrell, W. M., et al. (2010), Modification of the plasma in the near-vicinity of Enceladus by the enveloping dust, *Geophys. Res. Lett.*, *37*, L20202, doi:10.1029/2010GL044768.

Fleshman, B. L., P. A. Delamere, and F. Bagenal (2010), A sensitivity study of the Enceladus torus, *J. Geophys. Res.*, *115*, E04007, doi:10.1029/2009JE003372.

Gurnett, D. A., A. M. Persoon, W. S. Kurth, J. B. Groene, T. F. Averkamp, M. K. Dougherty, and D. J. Southwood (2007), The variable rotation period of the inner region of Saturn's plasma disk, *Science*, *316*, 442, doi:10.1126/science.1138562.

Gurnett, D. A., et al. (2011), Auroral hiss, electron beams and standing Alfvén wave currents near Saturn's moon Enceladus, *Geophys. Res. Lett.*, *38*, L06102, doi:10.1029/2011GL046854.

Gustafsson, G., and J.-E. Wahlund (2010), Electron temperatures in Saturn's plasma disc, *Planet. Space Sci.*, *58*, 1018–1025, doi:10.1016/j.pss.2010.03.007.

Hansen, C. J., L. Esposito, A. I. F. Stewart, J. Colwell, A. Hendrix, W. Pryor, D. Shemansky, and R. West (2006), Enceladus' water vapor plume, *Science*, *311*, 1422–1425, doi:10.1126/science.1121254.

Hansen, C. J., et al. (2008), Water vapour jets inside the plume of gas leaving Enceladus, *Nature*, *456*, 477–479, doi:10.1038/nature07542.

Hansen, C. J., D. E. Shemansky, L. W. Esposito, I. Stewart, and A. R. Hendrix (2010), The composition and structure of Enceladus' plume from a Cassini UVIS observation of a solar occultation, Abstract P23C-09 presented at 2010 Fall Meeting, AGU, San Francisco, Calif., 13–17 Dec.

Jia, Y.-D., C. T. Russell, K. K. Khurana, J. S. Leisner, Y. J. Ma, and M. K. Dougherty (2010a), Time-varying magnetospheric environment near Enceladus as seen by the Cassini magnetometer, *Geophys. Res. Lett.*, *37*, L09203, doi:10.1029/2010GL042948.

Jia, Y.-D., C. T. Russell, K. K. Khurana, Y. J. Ma, W. Kurth, and T. I. Gombosi (2010b), Interaction of Saturn's magnetosphere and its moons: 3. Time variation of the Enceladus plume, *J. Geophys. Res.*, *115*, A12243, doi:10.1029/2010JA015534.

Jia, Y.-D., C. T. Russell, K. K. Khurana, Y. J. Ma, D. Najib, and T. I. Gombosi (2010c), Interaction of Saturn's magnetosphere and its moons: 2. Shape of the Enceladus plume, *J. Geophys. Res.*, *115*, A04215, doi:10.1029/2009JA014873.

Jones, G. H., et al. (2009), Fine jet structure of electrically charged grains in Enceladus' plume, *Geophys. Res. Lett.*, *36*, L16204, doi:10.1029/2009GL038284.

Kempf, S., U. Beckmann, and J. Schmidt (2010), How the Enceladus dust plume feeds Saturn's E ring, *Icarus*, *206*(2), 446–457, doi:10.1016/j.icarus.2009.09.016.

Khurana, K. K., M. K. Dougherty, C. T. Russell, and J. S. Leisner (2007), Mass loading of Saturn's magnetosphere near Enceladus, *J. Geophys. Res.*, *112*, A08203, doi:10.1029/2006JA012110.

Kriegel, H., S. Simon, J. Mueller, U. Motschmann, J. Saur, K.-H. Glassmeier, and M. Dougherty (2009), The plasma interaction of

Enceladus: 3d hybrid simulations and comparison with Cassini MAG data, *Planet. Space Sci.*, *57*(14–15), 2113–2122, doi:10.1016/j.pss.2009.09.025.

Motschmann, U., and E. Kührt (2006), Interaction of the solar wind with weak obstacles: Hybrid simulations for weakly active comets and for Mars, *Space Sci. Rev.*, *122*, 197–208, doi:10.1007/s11214-006-6218-2.

Müller, J., S. Simon, U. Motschmann, K.-H. Glassmeier, J. Saur, J. Schüle, and G. J. Pringle (2010), Magnetic field fossilization and tail reconfiguration in titan's plasma environment during a magnetopause passage: 3d adaptive hybrid code simulations, *Planet. Space Sci.*, *58*(12), 1526–1546, doi:10.1016/j.pss.2010.07.018.

Müller, J., S. Simon, U. Motschmann, J. Schüle, K.-H. Glassmeier, and G. J. Pringle (2011), A.I.K.E.F.: Adaptive hybrid model for space plasma simulations, *Comput. Phys. Commun.*, *182*(4), 946–966, doi:10.1016/j.cpc.2010.12.033.

Neubauer, F. M. (1980), Nonlinear standing Alfven wave current system at Io: Theory, *J. Geophys. Res.*, *85*, 1171–1178, doi:10.1029/JA085iA03p01171.

Neubauer, F. M. (1998), The sub-Alfvénic interaction of the Galilean satellites with the Jovian magnetosphere, *J. Geophys. Res.*, *103*, 19,843–19,866, doi:10.1029/97JE03370.

Omidi, N., C. T. Russell, R. L. Tokar, and J. S. Leisner (2010), Hybrid simulations of the plasma environment around Enceladus, *J. Geophys. Res.*, *115*, A05212, doi:10.1029/2009JA014391.

Roussos, E., et al. (2008), Plasma and fields in the wake of Rhea: 3-D hybrid simulation and comparison with Cassini data, *Ann. Geophys.*, *26*, 619–637, doi:10.5194/angeo-26-619-2008.

Saur, J., F. M. Neubauer, D. F. Strobel, and M. E. Summers (1999), Three-dimensional plasma simulation of Io's interaction with the Io plasma torus: Asymmetric plasma flow, *J. Geophys. Res.*, *104*(A11), 25,105–25,126, doi:10.1029/1999JA900304.

Saur, J., F. M. Neubauer, D. F. Strobel, and M. E. Summers (2002), Interpretation of Galileo's Io plasma and field observations: I0, I24, and I27 flybys and close polar passes, *J. Geophys. Res.*, *107*(A12), 1422, doi:10.1029/2001JA005067.

Saur, J., F. M. Neubauer, and N. Schilling (2007), Hemisphere coupling in Enceladus' asymmetric plasma interaction, *J. Geophys. Res.*, *112*, A11209, doi:10.1029/2007JA012479.

Saur, J., N. Schilling, F. M. Neubauer, D. F. Strobel, S. Simon, M. K. Dougherty, C. T. Russell, and R. T. Pappalardo (2008), Evidence for temporal variability of Enceladus' gas jets: Modeling of Cassini observations, *Geophys. Res. Lett.*, *35*, L20105, doi:10.1029/2008GL035811.

Shafiq, M., J.-E. Wahlund, M. Morooka, W. Kurth, and W. Farrell (2011), Characteristics of the dust-plasma interaction near Enceladus' south pole, *Planet. Space Sci.*, *59*(1), 17–25, doi:10.1016/j.pss.2010.10.006.

Simon, S., A. Bößwetter, T. Bagdonat, U. Motschmann, and K.-H. Glassmeier (2006), Plasma environment of Titan: a 3-D hybrid simulation study, *Ann. Geophys.*, *24*(3), 1113–1135, doi:10.5194/angeo-24-1113-2006.

Simon, S., A. Bößwetter, T. Bagdonat, U. Motschmann, and J. Schuele (2007), Three-dimensional multispecies hybrid simulation of Titan's highly variable plasma environment, *Ann. Geophys.*, *25*(1), 117–144, doi:10.5194/angeo-25-117-2007.

Simon, S., J. Saur, F. M. Neubauer, U. Motschmann, and M. K. Dougherty (2009), Plasma wake of Tethys: Hybrid simulations versus Cassini MAG data, *Geophys. Res. Lett.*, *36*, L04108, doi:10.1029/2008GL036943.

Simon, S., J. Saur, H. Kriegel, F. M. Neubauer, U. Motschmann, and M. K. Dougherty (2011), Influence of negatively charged plume grains and hemisphere coupling currents on the structure of Enceladus' Alfvén wings: Analytical modeling of Cassini magnetometer observations, *J. Geophys. Res.*, *116*, A04221, doi:10.1029/2010JA016338.

Sittler, E. C., et al. (2006), Cassini observations of Saturn's inner plasmasphere: Saturn orbit insertion results, *Planet. Space Sci.*, *54*, 1197–1210, doi:10.1016/j.pss.2006.05.038.

Smith, H. T., R. E. Johnson, M. E. Perry, D. G. Mitchell, R. L. McNutt, and D. T. Young (2010), Enceladus plume variability and the neutral gas densities in Saturn's magnetosphere, *J. Geophys. Res.*, *115*, A10252, doi:10.1029/2009JA015184.

Spahn, F., et al. (2006), Cassini dust measurements at Enceladus and implications for the origin of the *E ring, Science*, *311*, 1416–1418, doi:10.1126/science.1121375.

Spencer, J. R., et al. (2006), Cassini encounters Enceladus: Background and the discovery of a south polar hot spot, *Science*, *311*, 1401–1405, doi:10.1126/science.1121661.

Spitale, J. N., and C. C. Porco (2007), Association of the jets of Enceladus with the warmest regions on its south-polar fractures, *Nature*, *449*, 695–697, doi:10.1038/nature06217.

Tenishev, V., M. R. Combi, B. D. Teolis, and J. H. Waite (2010), An approach to numerical simulation of the gas distribution in the atmosphere of Enceladus, *J. Geophys. Res.*, *115*, A09302, doi:10.1029/2009JA015223.

Teolis, B. D., M. E. Perry, B. A. Magee, J. Westlake, and J. H. Waite (2010), Detection and measurement of ice grains and gas distribution in the Enceladus plume by Cassini's Ion Neutral Mass Spectrometer, *J. Geophys. Res.*, *115*, A09222, doi:10.1029/2009JA015192.

Tian, F., A. I. F. Stewart, O. B. Toon, K. W. Larsen, and L. W. Esposito (2007), Monte Carlo simulations of the water vapor plumes on Enceladus, *Icarus*, *188*, 154–161, doi:10.1016/j.icarus.2006.11.010.

Tokar, R. L., et al. (2006), The interaction of the atmosphere of Enceladus with Saturn's plasma, *Science*, *311*, 1409–1412, doi:10.1126/science.1121061.

Tokar, R. L., et al. (2008), Cassini detection of water-group pick-up ions in the Enceladus torus, *Geophys. Res. Lett.*, *35*, L14202, doi:10.1029/2008GL034749.

Tokar, R. L., R. E. Johnson, M. F. Thomsen, R. J. Wilson, D. T. Young, F. J. Crary, A. J. Coates, G. H. Jones, and C. S. Paty (2009), Cassini detection of Enceladus' cold water-group plume ionosphere, *Geophys. Res. Lett.*, *36*, L13203, doi:10.1029/2009GL038923.

Wahlund, J.-E., et al. (2005), The inner magnetosphere of Saturn: Cassini RPWS cold plasma results from the first encounter, *Geophys. Res. Lett.*, *32*, L20S09, doi:10.1029/2005GL022699.

Wahlund, J.-E., et al. (2009), Detection of dusty plasma near the E-ring of Saturn, *Planet. Space Sci.*, *57*, 1795–1806, doi:10.1016/j.pss.2009.03.011.

Waite, J. H., et al. (2006), Cassini Ion and Neutral Mass Spectrometer: Enceladus plume composition and structure, *Science*, *311*, 1419–1422, doi:10.1126/science.1121290.

Waite, J. H., Jr., et al. (2009), Liquid water on Enceladus from observations of ammonia and 40Ar in the plume, *Nature*, *460*, 487–490, doi:10.1038/nature08153.

Wiehle, S., et al. (2011), First lunar wake passage of ARTEMIS: Discrimination of wake effects and solar wind fluctuations by 3D hybrid simulations, *Planet. Space Sci.*, *59*, 661–671, doi:10.1016/j.pss.2011.01.012.

Wilson, R. J., R. L. Tokar, and M. G. Henderson (2009), Thermal ion flow in Saturn's inner magnetosphere measured by the Cassini plasma spectrometer: A signature of the Enceladus torus?, *Geophys. Res. Lett.*, *36*, L23104, doi:10.1029/2009GL040225.

Yaroshenko, V. V., S. Ratynskaia, J. Olson, N. Brenning, J. Wahlund, M. Morooka, W. S. Kurth, D. A. Gurnett, and G. E. Morfill (2009), Characteristics of charged dust inferred from the Cassini RPWS measurements in the vicinity of Enceladus, *Planet. Space Sci.*, *57*, 1807–1812, doi:10.1016/j.pss.2009.03.002.

M. K. Dougherty, Space and Atmospheric Physics Group, Blackett Laboratory, Imperial College London, Exhibition Road, London SW7 2BZ, UK.

D. A. Gurnett and A. M. Persoon, Department of Physics and Astronomy, University of Iowa, Iowa City, IA 52242-1479, USA.

H. Kriegel and U. Motschmann, Institute for Theoretical Physics, TU Braunschweig, Mendelssohnstr. 3, D-38106 Braunschweig, Germany. (h.kriegel@tu-bs.de)

F. M. Neubauer, J. Saur, and S. Simon, Institute of Geophysics and Meteorology, University of Cologne, Albertus Magnus Platz, D-50923 Cologne, Germany.